J. Fluid Mech. (2009), *vol.* 639, *pp.* 343–372.
doi:10.1017/S002211200999108X

Topological structure of shock induced vortex breakdown

SHUHAI ZHANG[1]†, HANXIN ZHANG[2] AND CHI-WANG SHU[3]‡¶

[1]State Key Laboratory of Aerodynamics, China Aerodynamics Research and Development Centre, Mianyang, Sichuan 621000, China

[2]China Aerodynamics Research and Development Centre, Mianyang, Sichuan 621000, China

[3]Division of Applied Mathematics, Brown University, Providence, RI 02912, USA

(Received 18 February 2009; revised 1 July 2009; accepted 3 July 2009; first published online 19 October 2009)

Using a combination of critical point theory of ordinary differential equations and numerical simulation for the three-dimensional unsteady Navier–Stokes equations, we study possible flow structures of the vortical flow, especially the unsteady vortex breakdown in the interaction between a normal shock wave and a longitudinal vortex. The topological structure contains two parts. One is the sectional streamline pattern in the cross-section perpendicular to the vortex axis. The other is the sectional streamline pattern in the symmetrical plane. In the cross-section perpendicular to the vortex axis, the sectional streamlines have spiral or centre patterns depending on a function $\lambda(x,t)=1/\rho(\partial\rho/\partial t+\partial\rho u/\partial x)$, where x is the coordinate corresponding to the vortex axis. If $\lambda>0$, the sectional streamlines spiral inwards in the near region of the centre. If $\lambda<0$, the sectional streamlines spiral outwards in the same region. If $\lambda=0$, the sectional streamlines form a nonlinear centre. If λ changes its sign along the vortex axis, one or more limit cycles appear in the sectional streamlines in the cross-section perpendicular to the vortex axis. Numerical simulation for two typical cases of shock induced vortex breakdown (Erlebacher, Hussaini & Shu, *J. Fluid Mech.*, vol. 337, 1997, p. 129) is performed. The onset and time evolution of the vortex breakdown are studied. It is found that there are more limit cycles for the sectional streamlines in the cross-section perpendicular to the vortex axis. In addition, we find that there are quadru-helix structures in the tail of the vortex breakdown.

1. Introduction

Vortex breakdown characterizes an abrupt change of the vortex structure, which is a crucial element in many applications. Even though the occurrence of vortex breakdown on the lee side of a delta wing may disturb the lift and drag characteristics leading to poor controllability, it may also be useful in many other applications. For instance, vortex breakdown has often been proposed as a mechanism for rapid dissipation of the tip vortex shed from a large aircraft which may limit the frequency of take-off and landing at major airports. In the area of combustion, the swirling flow

† Supported by the Chinese National Natural Science Foundation grants 10572146 and 10772193 and 973 program 2009CB724104.

‡ Supported by NSF grant DMS-0809086 and ARO grant W911NF-08-1-0520.

¶ Email address for correspondence: shu@dam.brown.edu

is frequently employed to enhance mixing and the breakdown region may be used to stabilize the combustion flame.

The phenomenon of vortex breakdown was first observed by Werle (Werle 1954) in 1954 in a water tunnel. Since then, vortex breakdown has been extensively studied including experiments (Sarpkaya 1971; Faler & Leibovich 1977; Escudier 1984; Brücker & Althaus 1995; Klass, Schröder & Thomer 2005), numerical simulations (Kandil, Kandil & Liu 1992; Spall 1996; Zhang, Zhang & Zhu 1996, 1997; Krause, Thomer & Schröder 2003; Klass *et al.* 2005) and theoretical analysis (Hall 1961, 1967; Benjamin 1962; Howard & Gupta 1962; Bossel 1969; Lessen, Singh & Paillet 1974; Blackmore 1994; Brøns *et al.* 2007; Blackmore, Brøns & Goullet 2008). Based on experimental observation, Sarpkaya classified vortex breakdown into three types: bubble, spiral and double helix (Sarpkaya 1971). Faler and Leibovich (Faler & Leibovich 1977) found that there are six distinct types of vortex breakdown which contain the three modes described by Sapakaya and three more modes. The most common modes might be the bubble type and the spiral type, which can be found in almost all problems of vortex breakdown ranging from low Reynolds number flow in a swirl tube (Sarpkaya 1971; Faler & Leibovich 1977) or container (Escudier 1984) to the high Reynolds number vortical flow over delta-wings (Zhang, Zhang & Zhu 1996, 1997). Numerical simulation (Spall 1996) and experimental study (Brücker & Althaus 1995) found that the vortex breakdown can change from one mode to another under certain conditions. To study the flow structure in the breakdown region of bubble type breakdown, a dynamical model was derived by Blackmore (Blackmore 1994). Blackmore et al. also proposed a coaxial vortex ring model (Blackmore *et al.* 2008). To reveal the mechanism of the vortex breakdown, three different theories have been developed. They are the concept of a critical state (Benjamin 1962; Bossel 1969), analogy to boundary layer separation (Hall 1961, 1967) and hydrodynamic instability (Howard & Gupta 1962; Lessen *et al.* 1974). However, there still is not a universally accepted theory that can explain all the phenomena of vortex breakdown. More details can be found in the review papers (Leibovich 1978; Delery 1994; Kalkhoran & Smart 2000).

Enhancing mixing is an important application of vortex breakdown. In this area, the topological structure may play a very important role for the mixing efficiency. There have been many studies on the topological structure of the swirling flow and vortex breakdown. In 1995, Zhang (Zhang 1995) studied the topological structure of a steady vortex using the critical point theory of ordinary differential equations. He concluded that the sectional streamline pattern in the cross-section perpendicular to the vortex axis can be characterized by the function $\lambda(x) = 1/\rho(\partial \rho u/\partial x)$. Here, x represents the position along the vortex axis. If $\lambda > 0$, the sectional streamlines in the near region of the vortex core spiral inwards. If $\lambda < 0$, the sectional streamlines in this region spiral outwards. If λ changes its sign along the vortex axis x, one or more limit cycles appear in the sectional streamlines in the cross-section perpendicular to the vortex axis. In the case of isentropic flow, the function $\lambda(x)$ can be written as $\lambda(x) = (M_x^2 - 1)(1/\rho u)(\partial p/\partial x)$ where M_x is the Mach number along the vortex axis. Hence, it is found that there is an essential difference between supersonic and subsonic vortex flows. In the adverse pressure region, the supersonic vortex spirals inwards while the subsonic vortex spirals outwards. In the favourable pressure region, the supersonic vortex spirals outwards while the subsonic vortex spirals inwards. Therefore, vortex breakdown takes place in the adverse pressure region for a subsonic vortex. However, a supersonic vortex cannot break down unless there is a shock.

Numerical simulation for the vortical transonic and supersonic flows demonstrates the validity of the above results (Zhang *et al.* 1996, 1997). In the simulation, one or two limit cycles were found in the sectional streamlines in the cross-section perpendicular to the vortex axis and there are similar experimental results (Delery 1994, figure 28 on page 29). Using a bifurcation theory of two-dimensional dynamical systems, Brøns, Voigt & Sørensen (1999) studied the streamline topology of steady axisymmetric vortex breakdown in a cylinder with co- and counter-rotating end-covers. The study showed that all observed bifurcations can be completely described by normal forms. A classification of the steady pattern of the flow is obtained. Based on the notion of structural instability of dynamical system and fully three-dimensional simulations, Brøns *et al.* (2007) concluded that the structural instability of the axisymmetric bubble results in the complicated open bubble structure incompatible with axisymmetry.

However, both numerical simulation and experiment results reveal that the flow in the breakdown region is unsteady. A typical example is the vortex breakdown in the interaction of a shock wave and a longitudinal vortex which was systemically studied by Erlebacher, Hussaini & Shu (1997) through solving the axisymmetric Euler equations with a third order accurate essentially non-oscillatory (ENO) scheme. Numerical simulation shows that an oblique shock wave generated by the interaction continuously moves upwards. A breakdown point, which just follows the intersection of the oblique shock wave and vortex axis, continuously moves upwards. Therefore, the flow field in the breakdown region is unsteady, hence the topological structure may be different from that in the steady case. The purpose of this paper is to study the topological structure of unsteady vortical flow. Critical point theory is utilized, and direct numerical simulation for the full three-dimensional unsteady Navier–Stokes equations by a fifth order weighted essentially non-oscillatory (WENO) scheme is performed to study the onset and time evolution of the topological structure of the vortex breakdown in the shock longitudinal vortex interaction.

This paper is organized as follows. Section 2 contains an analysis of the topological structure of the vortex flow. The sectional streamline patterns in the cross-section perpendicular to the vortex axis and in the symmetrical plane are analysed. Section 3 contains numerical simulation results of vortex breakdown for the interaction of a shock wave and a longitudinal vortex. Two typical cases are simulated. One is out of the breakdown region and the other is a typical case inside the breakdown region in Erlebacher *et al.* (1997). Comparison between the numerical results and the topological analysis is performed. Section 4 contains our concluding remarks.

2. Topological analysis of the vortical flow

The basic idea of a topological approach to fluid mechanics is to analyse the trajectories of the ordinary differential equations $\dot{X} = U$, where U is the velocity field.

We choose an orthogonal coordinate system (x, y, z), where the axis x is the same as the vortex axis. The axes y and z are in the cross-section perpendicular to the vortex axis. u, v and w are the velocity components corresponding to the directions of x, y and z respectively. The flow satisfies the continuity equation

$$\frac{\partial \rho}{\partial t} + \frac{\partial \rho u}{\partial x} + \frac{\partial \rho v}{\partial y} + \frac{\partial \rho w}{\partial z} = 0, \tag{2.1}$$

and the Euler equations for the velocity

$$\left.\begin{aligned}\frac{\partial u}{\partial t}+u\frac{\partial u}{\partial x}+v\frac{\partial u}{\partial y}+w\frac{\partial u}{\partial z}&=-\frac{1}{\rho}\frac{\partial p}{\partial x},\\ \frac{\partial v}{\partial t}+u\frac{\partial v}{\partial x}+v\frac{\partial v}{\partial y}+w\frac{\partial v}{\partial z}&=-\frac{1}{\rho}\frac{\partial p}{\partial y},\\ \frac{\partial w}{\partial t}+u\frac{\partial w}{\partial x}+v\frac{\partial w}{\partial y}+w\frac{\partial w}{\partial z}&=-\frac{1}{\rho}\frac{\partial p}{\partial z}.\end{aligned}\right\} \tag{2.2}$$

Here, we neglect the viscous terms due to the high Reynolds number of supersonic flow and since we are only looking for qualitative characters of a topological analysis. We also neglect the energy equation since it is not used in the analysis.

Because the vortex axis is a streamline, and assuming the flow is axisymmetric, we have the boundary conditions on the vortex axis

$$v(x,0,0)=w(x,0,0)=0. \tag{2.3}$$

The velocity in the near region of the vortex axis can be expressed by a Taylor expansion

$$\left.\begin{aligned}u(x,y,z)&=u_0+\frac{\partial u}{\partial x}x+\frac{\partial u}{\partial y}y+\frac{\partial u}{\partial z}z+O(x^2,y^2,z^2),\\ v(y,z)&=\frac{\partial v}{\partial y}y+\frac{\partial v}{\partial z}z+O(y^2,z^2),\\ w(y,z)&=\frac{\partial w}{\partial y}y+\frac{\partial w}{\partial z}z+O(y^2,z^2).\end{aligned}\right\} \tag{2.4}$$

Here and below, all the spatial derivatives $\partial u/\partial x$, $\partial u/\partial y$, $\partial u/\partial z$, $\partial v/\partial y$, $\partial v/\partial z$, $\partial w/\partial y$ and $\partial w/\partial z$ are evaluated on the vortex axis.

The streamlines can be represented by the ordinary differential equation (Brøns *et al.* 2007)

$$\left.\begin{aligned}\frac{\mathrm{d}x}{\mathrm{d}t}&=u,\\ \frac{\mathrm{d}y}{\mathrm{d}t}&=v,\\ \frac{\mathrm{d}z}{\mathrm{d}t}&=w.\end{aligned}\right\} \tag{2.5}$$

Equation (2.5) is a dynamical system which can describe the flow patterns near a critical point in the flow field. There has been a long history in the literature of using a dynamic system approach to study the streamline pattern. Most studies are on streamline patterns in the vicinity of steady and unsteady separation (Hunt *et al.* 1978; Tobak & Peake 1982; Perry & Chong 1986; Haller 2004; Surana, Grunberg & Haller 2006). Brøns et al. studied the streamline topology of steady axisymmetric vortex breakdown in a cylinder with co- and counter-rotating end-covers (Brøns *et al.* 1999). The study showed that all observed bifurcations can be completely described by normal forms. A classification of the steady pattern of the flow is obtained by a combination of bifurcation theory and numerical simulation.

Here, we use (2.5) to study the streamline pattern of a swirling flow, especially in the cross-section perpendicular to the vortex axis as well as in the symmetric plane.

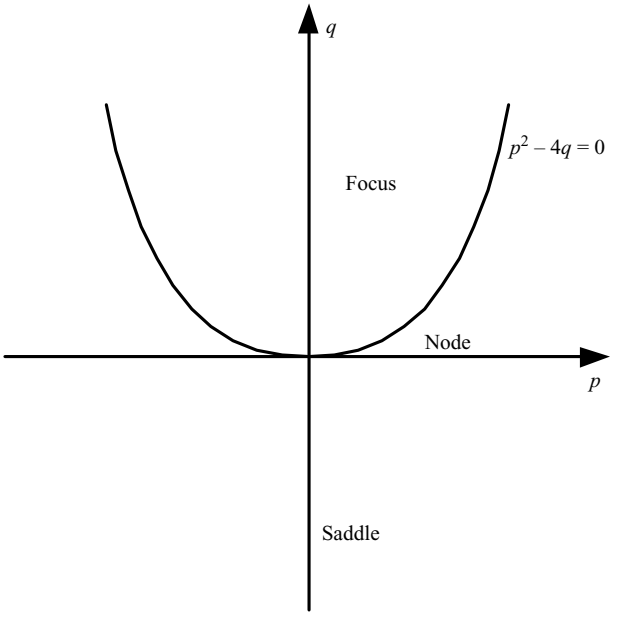

FIGURE 1. The pattern of a critical point.

2.1. *Sectional streamline patterns in the cross-section perpendicular to the vortex axis*

In the cross-section perpendicular to the vortex axis, the sectional streamline can be described by

$$\frac{\mathrm{d}z}{\mathrm{d}y} = \frac{w}{v} = \frac{\dfrac{\partial w}{\partial y}y + \dfrac{\partial w}{\partial z}z + O(y^2, z^2)}{\dfrac{\partial v}{\partial y}y + \dfrac{\partial v}{\partial z}z + O(y^2, z^2)}. \tag{2.6}$$

If we neglect the higher order terms, it can be rewritten as

$$\frac{\mathrm{d}z}{\mathrm{d}y} = \frac{w}{v} = \frac{\dfrac{\partial w}{\partial y}y + \dfrac{\partial w}{\partial z}z}{\dfrac{\partial v}{\partial y}y + \dfrac{\partial v}{\partial z}z}. \tag{2.7}$$

According to the critical point theory of ordinary differential equation (Crank, Martin & Melluish 1977), the sectional streamline pattern in the vicinity of the vortex axis depends mainly on two parameters: $p = -(\partial v/\partial y + \partial w/\partial z)$ and $q = \partial v/\partial y \times \partial w/\partial z - \partial v/\partial z \times \partial w/\partial y$. There are three kinds of critical points: saddle, node and focus. The classification of the critical point in the parameter plane is plotted in figure 1.

For a swirling flow, the sectional streamline pattern should be a focus in the near region of the vortex axis (Chong, Perry & Cantwell 1990). The spiral direction is determined by the function $\lambda(x, t)$ defined as

$$\lambda(x, t) = p = -\left(\frac{\partial v}{\partial y} + \frac{\partial w}{\partial z}\right)_o = \frac{1}{\rho}\left(\frac{\partial \rho}{\partial t} + \frac{\partial \rho u}{\partial x}\right)_o. \tag{2.8}$$

Here, we have used the continuity equation (2.1) and the boundary condition (2.3) on the vortex axis (the subscript 'o'). If $\lambda(x, t) > 0$, the sectional streamlines in the

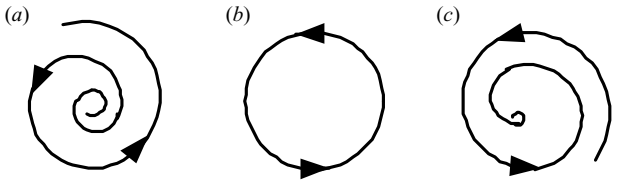

FIGURE 2. Schematic diagram of the sectional streamline topology in the cross-section perpendicular to the vortex axis. (*a*) $\lambda(x,t)<0$; (*b*) $\lambda(x,t)=0$; (*c*) $\lambda(x,t)>0$.

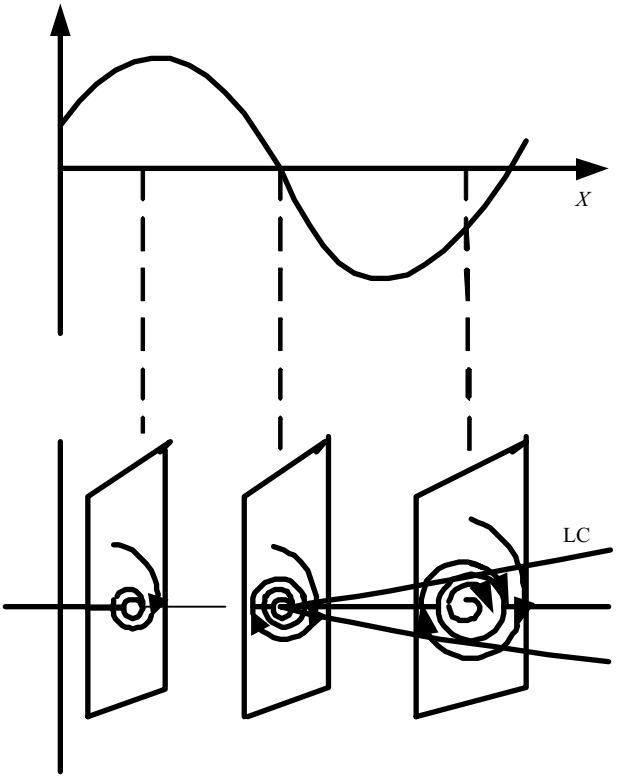

FIGURE 3. Schematic diagram of the sectional streamline topology in the cross-section and its relation with λ along the vortex axis. 'LC' refers to a limit cycle.

cross-section perpendicular to the vortex axis spiral inwards. If $\lambda(x,t)=0$, the sectional streamlines in this cross-section form a nonlinear centre. If $\lambda(x,t)<0$, the sectional streamlines in this cross-section spiral outwards. The sectional streamlines in the vicinity of the critical point are schematically shown in figure 2.

If the sectional streamlines far away from the vortex axis spiral inwards, which is the case for vortices generated by the separation such as those over a delta wing, one or more limit cycles appear in the cross-section perpendicular to the vortex axis as λ changes its sign (Crank *et al.* 1977). This is schematically shown in figure 3.

A limit cycle separates the swirling flow into two different regions. Hence, the appearance of limit cycles is not beneficial to the enhancement of mixing. Suppose the fuel is in the inner region of a vortex and the air is in the outer region, a limit cycle might separate the two kinds of fluids and prevent their mixing.

If the flow is steady, the first term on the right side of (2.8) vanishes, and the function λ can be rewritten as

$$\lambda(x) = \left(\frac{\partial u}{\partial x} + \frac{u}{\rho}\frac{\partial \rho}{\partial x}\right)_o. \tag{2.9}$$

If the flow is isentropic, $(\partial p/\partial \rho)_s = a^2$ where a is the sound speed of the fluid. Then we have

$$\lambda(x) = \left(\frac{\partial u}{\partial x} + \frac{u}{\rho a^2}\frac{\partial p}{\partial x}\right)_o. \tag{2.10}$$

The Euler equation on the vortex axis can be written as

$$u\frac{\partial u}{\partial x} = -\frac{1}{\rho}\frac{\partial p}{\partial x}. \tag{2.11}$$

At the points of $u_o \neq 0$, the function λ can be rewritten as

$$\lambda(x) = \frac{1}{(\rho u)_o}\left(M_x^2 - 1\right)\left(\frac{\partial p}{\partial x}\right)_o. \tag{2.12}$$

This equation is also obtained by Zhang in Zhang (1995).

From (2.12), we know that there is an essential difference between a supersonic vortex and a subsonic vortex. For a subsonic swirling flow, the sectional streamlines in the vicinity of the vortex axis spiral inwards in the locally favourable pressure region and they spiral outwards in the locally adverse pressure region. However, for a supersonic swirling flow, the sectional streamlines in the vicinity of the vortex axis spiral outwards in the locally favourable pressure region and they spiral inwards in the locally adverse pressure region.

2.2. *Sectional streamline pattern in the meridional plane*

In the meridional plane (the x–z plane), the sectional streamline can be described by

$$\left.\begin{aligned} \frac{\mathrm{d}x}{\mathrm{d}t} &= u_0 + \frac{\partial u}{\partial x}x + \frac{\partial u}{\partial z}z + O(x^2, z^2), \\ \frac{\mathrm{d}z}{\mathrm{d}t} &= \frac{\partial w}{\partial z}z + O(z^2). \end{aligned}\right\} \tag{2.13}$$

If $u_0 = 0$, the origin is a critical point. Keeping the linear term, the sectional streamline in the vicinity of the critical point can be represented by

$$\frac{\mathrm{d}z}{\mathrm{d}x} = \frac{w}{u} = \frac{\dfrac{\partial w}{\partial z}z}{\dfrac{\partial u}{\partial x} + \dfrac{\partial u}{\partial z}z}. \tag{2.14}$$

The two parameters to determine the character of the sectional streamline pattern in the vicinity of the critical point are $p = -(\partial u/\partial x + \partial w/\partial z)$ and $q = \partial u/\partial x \times \partial w/\partial z$. Because $p^2 - 4q = (\partial u/\partial x - \partial w/\partial z)^2 \geqslant 0$, the only possible critical point on the vortex axis in the meridional plane is a saddle or a node as shown in figure 4.

The pattern of critical points on the vortex axis in the meridional plane for an unsteady flow is different from that of a steady flow, which is a saddle (Brøns *et al.* 1999). In fact, if the flow is steady, $\partial \rho/\partial t = 0$. The continuity equation (2.1) can be

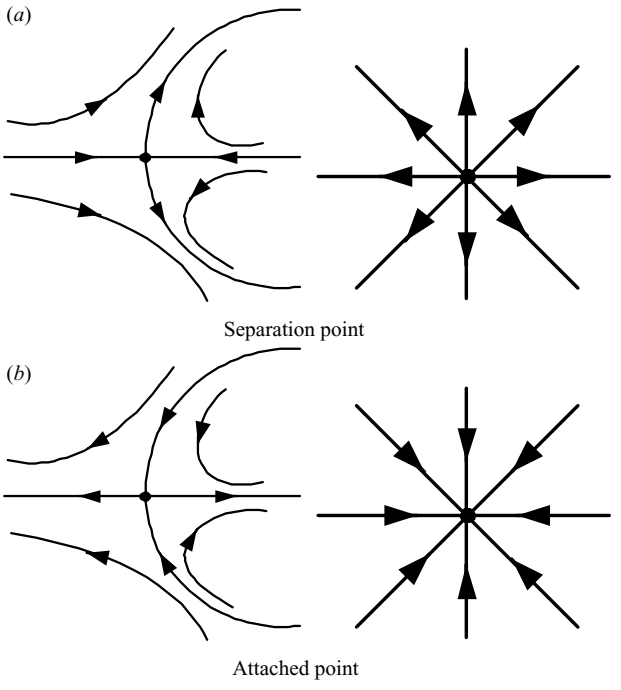

FIGURE 4. Schematic diagram of the sectional streamline topology in the meridional plane.

written as

$$\frac{\partial(\rho u)}{\partial x} + \frac{\partial(\rho v)}{\partial y} + \frac{\partial(\rho w)}{\partial z} = 0. \tag{2.15}$$

At a critical point, this becomes

$$\frac{\partial u}{\partial x} + \frac{\partial v}{\partial y} + \frac{\partial w}{\partial z} = 0. \tag{2.16}$$

The flow is incompressible in the near region of the critical point (Haller 2004).

At a non-degenerate critical point in the vortex axis of the meridional plane, $\partial w/\partial z = -\partial u/\partial x$ and $q = \partial u/\partial x \times \partial w/\partial z = -(\partial u/\partial z)^2 < 0$, hence the critical point is a saddle.

If $\partial w/\partial z = 0$, the origin is a degenerate critical point. Brøns *et al.* (1999) studied the streamline pattern near a degenerate critical point for the incompressible flow using the normal form theory and found there are six types of streamline patterns. Here, we replot these patterns in figure 5. Even though these patterns are obtained for the incompressible flow, they seem to be applicable also to the compressible flow, probably because the flow becomes approximately incompressible in the near region of a critical point, as in the steady case (Haller 2004).

3. Numerical simulation of shock-longitudinal vortex interaction

The fifth order finite difference WENO scheme (Jiang & Shu 1996; Zhang, Zhang & Shu 2005, 2006) is used to simulate the following three-dimensional unsteady Navier–Stokes equations for the conservative variables:

$$U_t + F(U)_x + G(U)_y + H(U)_z = \frac{1}{Re}(F_v(U)_x + G_v(U)_y + H_v(U)_z), \tag{3.1}$$

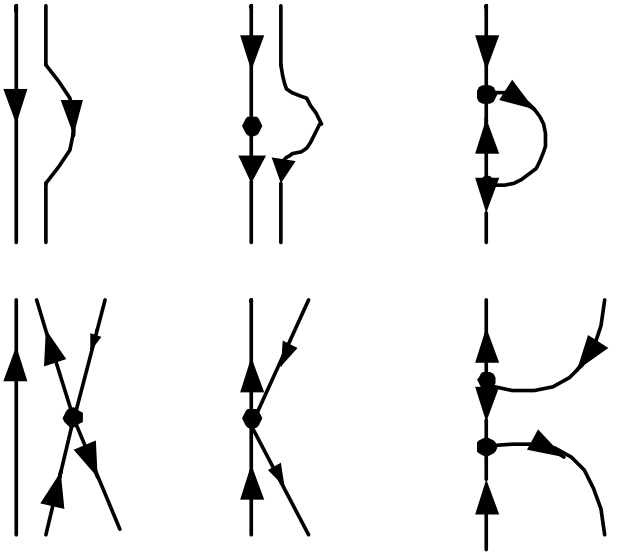

FIGURE 5. Streamline patterns near a degenerate critical point from figure 3 in Brøns M., Voigt & Sørensen (1999).

where

$$U = (\rho, \rho u, \rho v, \rho w, e)^T, \quad F(U) = [\rho u, \rho u^2 + p, \rho uv, \rho uw, u(e+p)]^T,$$
$$G(U) = [\rho v, \rho uv, \rho v^2 + p, \rho vw, v(e+p)]^T,$$
$$H(U) = [\rho w, \rho uw, \rho vw, \rho w^2 + p, w(e+p)]^T,$$
$$F_v(U) = [0, \tau_{xx}, \tau_{xy}, \tau_{xz}, u\tau_{xx} + v\tau_{xy} + w\tau_{xz} + q_x]^T,$$
$$G_v(U) = [0, \tau_{xy}, \tau_{yy}, \tau_{yz}, u\tau_{xy} + v\tau_{yy} + w\tau_{yz} + q_y]^T,$$
$$H_v(U) = [0, \tau_{xz}, \tau_{yz}, \tau_{zz}, u\tau_{xz} + v\tau_{yz} + w\tau_{zz} + q_z]^T.$$

Here ρ is the density, (u, v, w) is the velocity, e is the total energy, p is the pressure, which is related to the total energy by $e = p/(\gamma - 1) + 1/2\rho(u^2 + v^2 + w^2)$, the ratio of specific heats $\gamma = 1.4$. Re is the Reynolds number defined by $Re = \rho_\infty u_\infty r_0/\mu_\infty$, where ρ_∞, u_∞ and μ_∞ are the density, speed and viscosity for the mean flow upstream of the shock wave, r_0 is the reference length scale which is chosen as the vortex core. τ_{ij} and q_i (where $i, j = 1$ for x, $i, j = 2$ for y and $i, j = 3$ for z) are the stress tensor and the heat flux, respectively, and are given by

$$\tau_{ij} = \mu\left(\frac{\partial u_i}{\partial x_j} + \frac{\partial u_j}{\partial x_i} - \frac{2}{3}\delta_{ij}\frac{\partial u_k}{\partial x_k}\right), \quad q_i = \frac{\mu}{(\gamma - 1)Pr}\frac{\partial T}{\partial x_i},$$

where, $Pr = 0.75$ is the Prandtl number, $\mu = T^{3/2}(1 + c)/(T + c)$ is viscosity computed by the Sutherland law, with $c = 110.4/T_\infty$ and $T_\infty = 300$, and $T = \gamma\frac{p}{\rho}$ is the temperature. In our simulation, we choose the Reynolds number $Re = 10^6$.

Following the simulation in Erlebacher *et al.* (1997), a stationary shock is initially located at the $x = 0$ plane. In the upstream of the shock ($x < 0$)

$$\rho = 1, \quad u_x = -\gamma^{1/2}M_1, \quad u_r = u_\theta = 0, \quad p = 1, \tag{3.2}$$

and the downstream mean solution is ($x > 0$)

$$\left.\begin{aligned} \rho &= \frac{(\gamma+1)M_1^2}{(\gamma-1)M_1^2+2}, \quad u_x = -\frac{\gamma^{1/2}\left((\gamma-1)M_1^2+2\right)}{(\gamma+1)M_1}, \\ u_r &= u_\theta = 0, \quad p = \frac{2\gamma M_1^2-(\gamma-1)}{\gamma+1}. \end{aligned}\right\} \tag{3.3}$$

An isentropic vortex is superimposed on the mean flow upstream of the shock. The axis of the vortex is along the x-axis ($y = z = 0$). Analytical forms of such vortices with arbitrary radial profiles are steady state solutions of the Euler equations. The perturbations of the azimuthal velocity u'_θ and the temperature associated with the vortex are given by

$$u'_\theta = \frac{\epsilon r}{2\pi} e^{0.5(1-r^2)}, \quad T' = -\frac{(\gamma-1)\epsilon^2}{8\gamma\pi^2 r_0^2} e^{(1-r^2)}, \tag{3.4}$$

where $r = \sqrt{y^2+z^2}$ is the radius to the vortex axis, r_0 is the vortex core radius and ϵ is a non-dimensional circulation at $r = 1$, related to the dimensional circulation Γ by

$$\epsilon = \frac{\Gamma}{r_0 c^*}. \tag{3.5}$$

The axial and radial velocity components u'_x and u'_r are zero, the entropy $S = \log(p/\rho^\gamma)$ is constant inside the vortex, and u'_θ is maximum at $r = 1$.

Erlebacher *et al.* (1997) systemically simulated the interaction of a normal shock and a longitudinal vortex using a third-order ENO scheme through solving the axisymmetrical Euler equations. The region for the shock induced vortex breakdown was obtained by a parameter study. This simulation revealed many features of shock dynamics and vortex breakdown. However, due to the axisymmetric limitation, it cannot predict the sectional streamline pattern in the cross-section perpendicular to the vortex axis. Neither can it reveal the instability of the azimuthal wave modes (Sanchez, Marques & Lopez 2002; Marques, Gelfgat & Lopez 2003) nor the azimuthal vorticity gradient (Kurosaka *et al.* 2006), which plays a very important role in vortex breakdown. Hence, the simulation for the full three-dimensional Navier–Stokes equations is necessary. In this paper, we do not repeat all the cases of the simulation in Erlebacher *et al.* (1997). We just simulate two typical cases to reveal the topological structure and the evolution of the vortex breakdown in a full three-dimensional setting. The first case corresponds to $M_1 = 1.2$ and $\epsilon = 4.5$, which is beyond the vortex breakdown region given by Erlebacher *et al.* (1997). The second case is a typical case involving vortex breakdown in Erlebacher *et al.* (1997) with $M_1 = 2$ and $\epsilon = 7$.

To validate our three-dimensional code, we perform an accuracy test for unsteady Navier–Stokes equations using an explicitly given smooth solution, similar to that in Zhang & Shu (2007). The designed order of accuracy is achieved in a mesh refinement study. Then, we compute the numerical result for the interaction of a normal shock wave and a longitudinal vortex with $M_1 = 2$ and $\epsilon = 7$ with different grid density. Figure 6 contains the distribution of pressure and Mach number on the vortex axis and a comparison among three different grids of the current three-dimensional code, as well as the result obtained from the axisymmetric Euler equation by a third-order ENO scheme in Erlebacher *et al.* (1997). The finest grid (Grid1) has $1600 \times 640 \times 640$ grid points, corresponding to the x, y and z directions respectively. The coarser grid (Grid2) has $800 \times 320 \times 320$ points, and the coarsest grid (Grid3) has $300 \times 120 \times 120$ points. The axisymmetric Euler equations are simulated by a grid

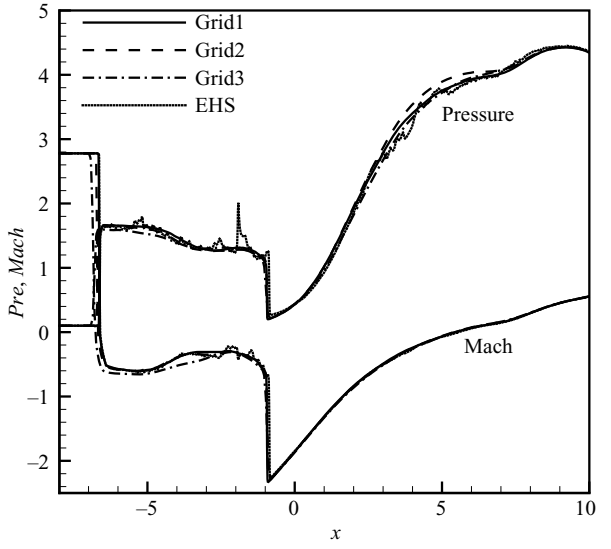

FIGURE 6. The distribution of pressure and Mach number along the vortex axis for different grids.

density of 1600×640 (EHS). The computational domain is set to be $x_l = -8$, $x_r = 10$, $y_l = z_l = -5$, $y_r = z_r = 5$. The comparison shows that a grid convergence is achieved. However, the grid convergence here does not imply that simulation results for all the cases in this paper are not related to the grid density. In fact, there are many small-scale structures, such as the critical point on the limit cycle and fluctuation of the velocity, pressure and density, which are very difficult to resolve and hence the results may be related to grid density.

To reveal the topological structure of a vortical flow, especially in the region of vortex breakdown, sectional streamlines in two cross-sections are plotted. One is the cross-section perpendicular to the vortex axis. Because the vortex axis in our numerical simulations is aligned with the x-axis, this cross-section is the y–z plane. The sectional streamlines in this cross-section exactly represent the path described by (2.6). The other is the meridional plane or the x–z plane. The sectional streamlines in the meridional plane exactly represent the path described by (2.13).

Plotting sectional streamlines is a common method to visualize flow structure for numerical results (Erlebacher *et al.* 1997; Kandil *et al.* 1992; Blackmore 1994; Zhang & Zhu 1997; Krause *et al.* 2003) and is used in the digital measuring experiment (Delery 1994). However, the interpretation of sectional streamlines should be given with care, as these are not real streamlines when there is a non-zero velocity component out of the plane. We will give more discussion about this point later in § 3.4.

3.1. *Case I*

Our first simulation case corresponds to $M_1 = 1.2$ and $\epsilon = 4.5$, which is beyond the region of shock induced vortex breakdown given by Erlebacher *et al.* (1997). However, in our simulation, we still observe vortex breakdown. In this case, the main difference between the two simulations is the size of the computational domain and the simulation time. In Erlebacher *et al.* (1997), the computational domain is chosen to be $x_l = -8$, $x_r = 10$, $r_m = 5$ and the simulation runs to $t = 11$.

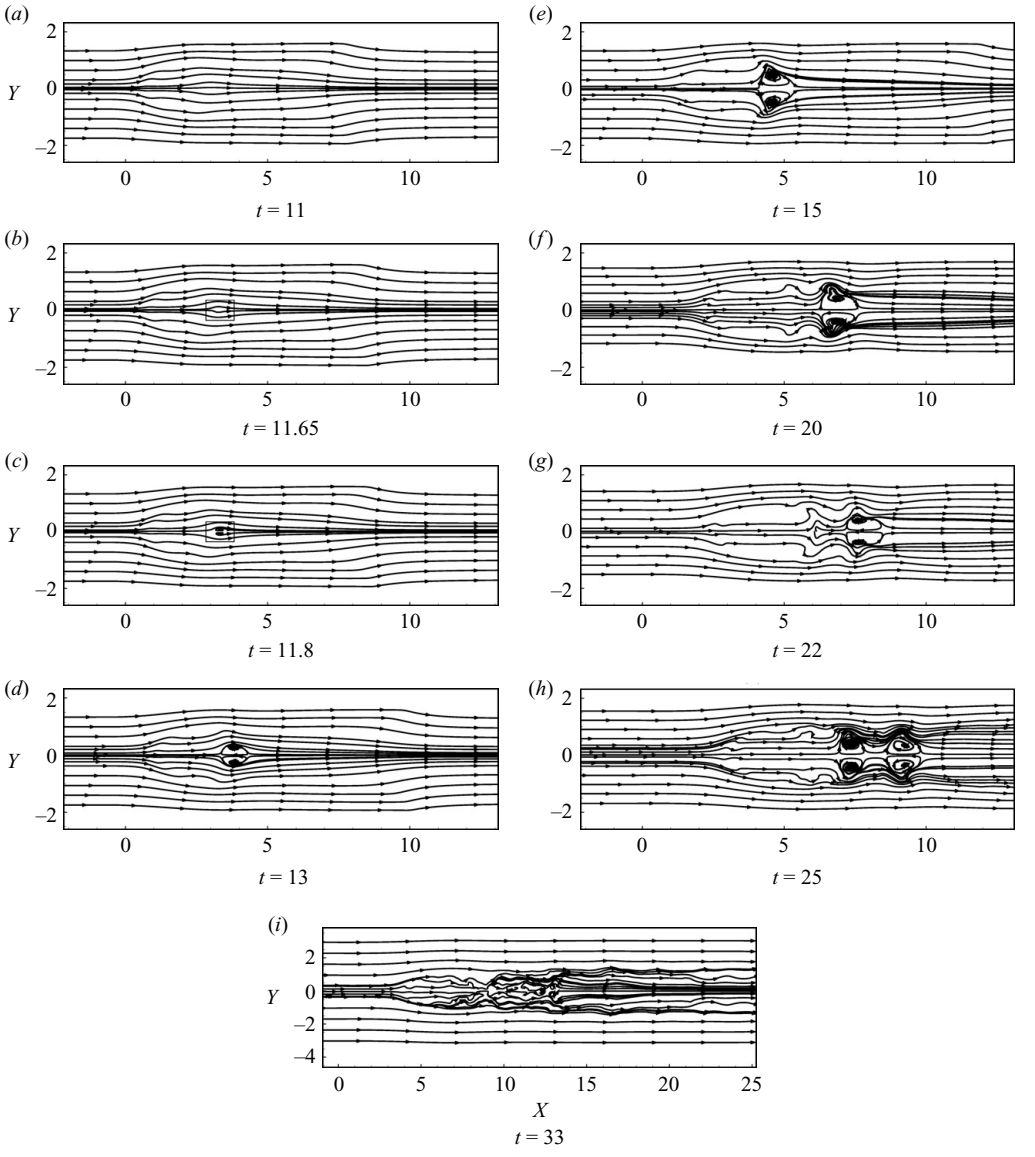

FIGURE 7. The onset and evolution of vortex breakdown for $M_1 = 1.2$ and $\epsilon = 4.5$.

In this paper, the computational domain is chosen as $x_l = -10$, $x_r = 28$, $y_l = z_l = -5$ and $y_r = z_r = 5$ and the simulation runs to $t = 50$. The grid density is $1600 \times 320 \times 320$.

3.1.1. *The topological structure in the meridional plane*

Figure 7 contains the sectional streamlines in the meridional plane at a series of typical times. At $t = 11$, in figure 7(a), there is no critical point on the vortex axis, neither is there a reversal flow region which could be seen as a criterion of vortex breakdown. Hence, the vortex has not broken down yet, coinciding with the result in Erlebacher *et al.* (1997). However, as time increases, the vortex changes its pattern dramatically. At $t = 11.65$, the sectional streamlines which are close to the vortex axis turn away from the axis near $x = 3.5$. As a result, the stream surface is swollen near this region, which is similar to the first pattern of Brøns *et al.* (1999) shown in figure 5,

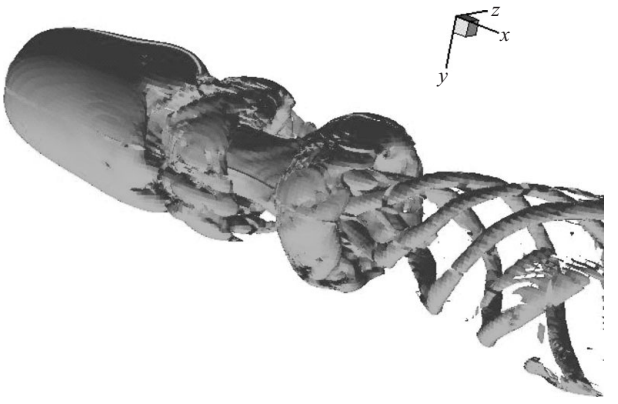

FIGURE 8. The iso-surface of vorticity $|\omega| = 3$ at $t = 25$ of Case I.

as can be seen in the boxed region in figure 7(*b*). At $t = 11.8$, a region of reversal axial flow appears. There are two saddle points on the vortex axis. One corresponds to separation and the other to attachment, which are the same with those in figure 4. This is the onset point of vortex breakdown. As time further evolves, the separation bubble becomes larger. At the time $t = 25$, a second reversal axial flow appears. As the vortex breakdown develops continuously, the two bubbles disappear, and there are a series of critical points on the vortex axis (see figure 7*i*).

Figure 8 is the iso-vorticity surface of $|\omega| = \sqrt{\omega_x^2 + \omega_y^2 + \omega_z^2}$, which was widely used to show vortex cores (Hussain & Hayakawa 1987; Bisset, Antonia & Browne 1990; Ruith *et al.* 2003). Jeong and Hussain (Jeong & Hussain 1995) concluded that the iso-vorticity surface at a sufficiently low level is a necessary but not sufficient condition to detect a tubular vortex coherent structure. From figure 8, we find that the breakdown has a quadru-helix structure, which does not seem to have been reported in previous studies. This structure is different from the double helix structure found by Sarpkaya (1971). It is similar to the two-tailed type 0 breakdown observed by Faler & Leibovich (1977). We will discuss it further in § 3.3.

3.1.2. *The sectional streamline pattern in the cross-section perpendicular to the vortex axis*

Based on our topological analysis in § 2, $\lambda(x, t) = 1/\rho(\partial\rho/\partial t + \partial\rho u/\partial x)$ is a key function to determine the sectional streamline pattern in the cross-section perpendicular to the vortex axis. The sign of $\lambda(x, t)$ decides the spiral direction of the sectional streamline in the vicinity of the vortex core. If $\lambda(x, t)$ changes sign along the vortex axis, there might be one or more limit cycles. Figure 9 is the distribution of $\lambda(x, t)$ along the vortex axis at time $t = 25$. Along the vortex axis, there are seven regions where $\lambda > 0$, which are represented by p_i, $(i = 1, 2, \ldots, 7)$, and six regions where $\lambda < 0$, which are represented by n_i, $(i = 1, 2, \ldots, 6)$. Figure 10 contains the sectional streamlines in the cross-section perpendicular to the vortex axis. Because the initial vortex is isentropic, $\lambda = 0$ in the undisturbed region. Hence, the sectional streamline forms a nonlinear centre in the undisturbed region. At the cross-section of $x = -0.125$, which is just before the initial shock wave, $\lambda = 0.026$, the sectional streamline in the vicinity of the vortex core spirals inwards which is shown in figure 10(*a*). At the cross-section of $x = 1.45$, $\lambda = -0.115$, the sectional streamline in the vicinity of the vortex core spirals outwards. From $x = -0.125$ to $x = 1.45$, the sign of λ changes from positive to negative, however, we do not observe a limit cycle.

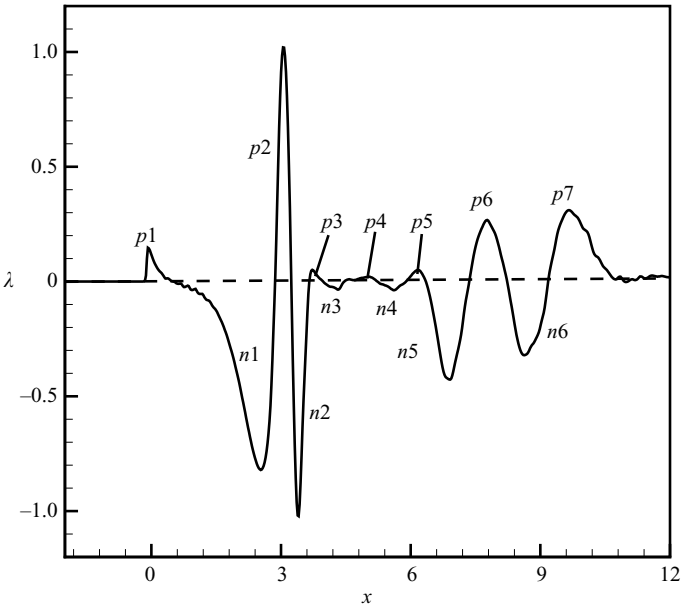

FIGURE 9. The distribution of λ on the vortex axis at $t = 25$ of Case I.

This might be due to the proximity to the shock region. Even though λ changes its sign, the sectional streamlines in both the near vortex core region and far region can change their spiral directions due to the shock wave, resulting in the lack of limit cycle. This phenomenon was also observed in a two-dimensional shock vortex interaction (Zhang *et al.* 2005). The spiral direction of the vortex is affected by the oscillation of the deformed shock wave. At the cross-section of $x = 3.025$, $\lambda = 0.985$, the sectional streamline in the vicinity of the vortex core spirals inwards which is shown in figure 10(c). From the cross-section $x = 1.45$ to $x = 3.025$, λ changes its sign and a limit cycle appears. Followed this, when x increases to $x = 3.7$, λ changes its sign twice, there are two more limit cycles which can be seen in figures 10(d) and 10(e). It is noted that not every change of the sign of λ could result in a limit cycle. Occasionally, the change of the sign of λ reduces the number of limit cycles. For instance, when x increases from 3.7 to 4.15 (see figures 10e and 10f), λ changes its sign from positive to negative, but there is no limit cycle added. Instead, one limit cycle disappears. This might be the result of a merging of the separated regions.

Based on the sectional streamlines in the meridional plane, we conclude that the vortex breakdown occurs at approximately $x = 5$ at $t = 25$, which can be seen in figure 7(h). From the cross-section of $x = 5.3875$, four small vortices appear in the circumferential direction, which is the result of the double Hopf bifurcation of the swirling flow (Sanchez *et al.* 2002; Marques *et al.* 2003). We deduce that this is the origin of the quadru-helix structure shown in figure 8 and we will discuss this further in § 3.3.

The sectional streamlines in figure 10 are mainly plotted in the cross-sections in the region of vortex breakdown, while the quadru-helix structure is observed by the vorticity iso-surface located in the tail of the vortex breakdown. To illustrate better this vortex quadru-helix structure, we plot in figure 11 the iso-surface of density as well as the sectional streamlines at the cross-section $x = 19.9$ which is in the tail of the vortex breakdown. The quadru-helix structure can be observed in the iso-surface of density, and each helix matches with a vortex in the sectional streamlines.

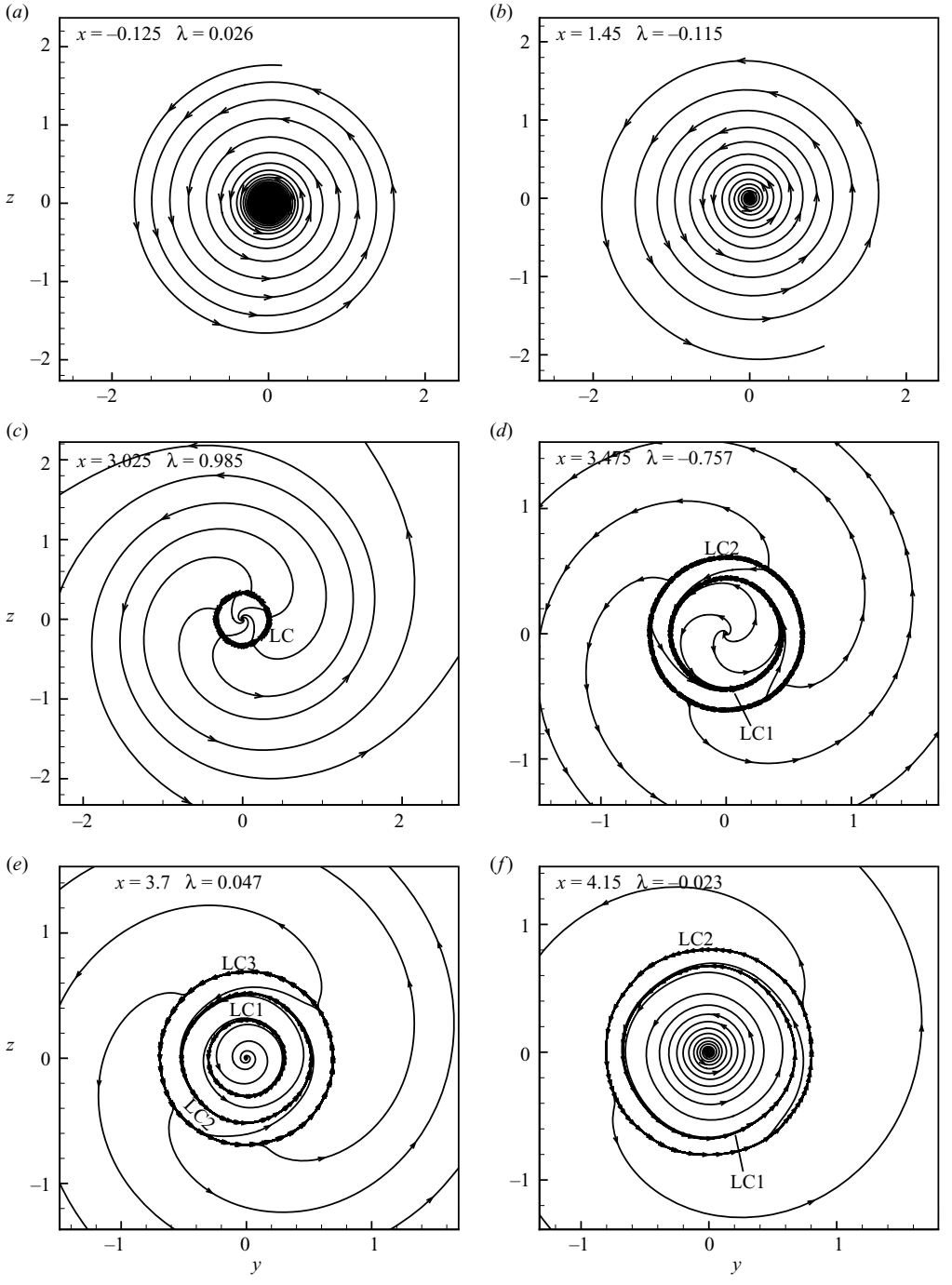

FIGURE 10. For caption see page 17

3.2. *Case II*

Our second case is a typical case of vortex breakdown in Erlebacher *et al.* (1997) with $M_1 = 2$ and $\epsilon = 7$. Erlebacher *et al.* (1997) gave the evolution of the vortex breakdown. Here, we will focus on the study of the topological structure, which is obtained by the finest grid $1600 \times 640 \times 640$.

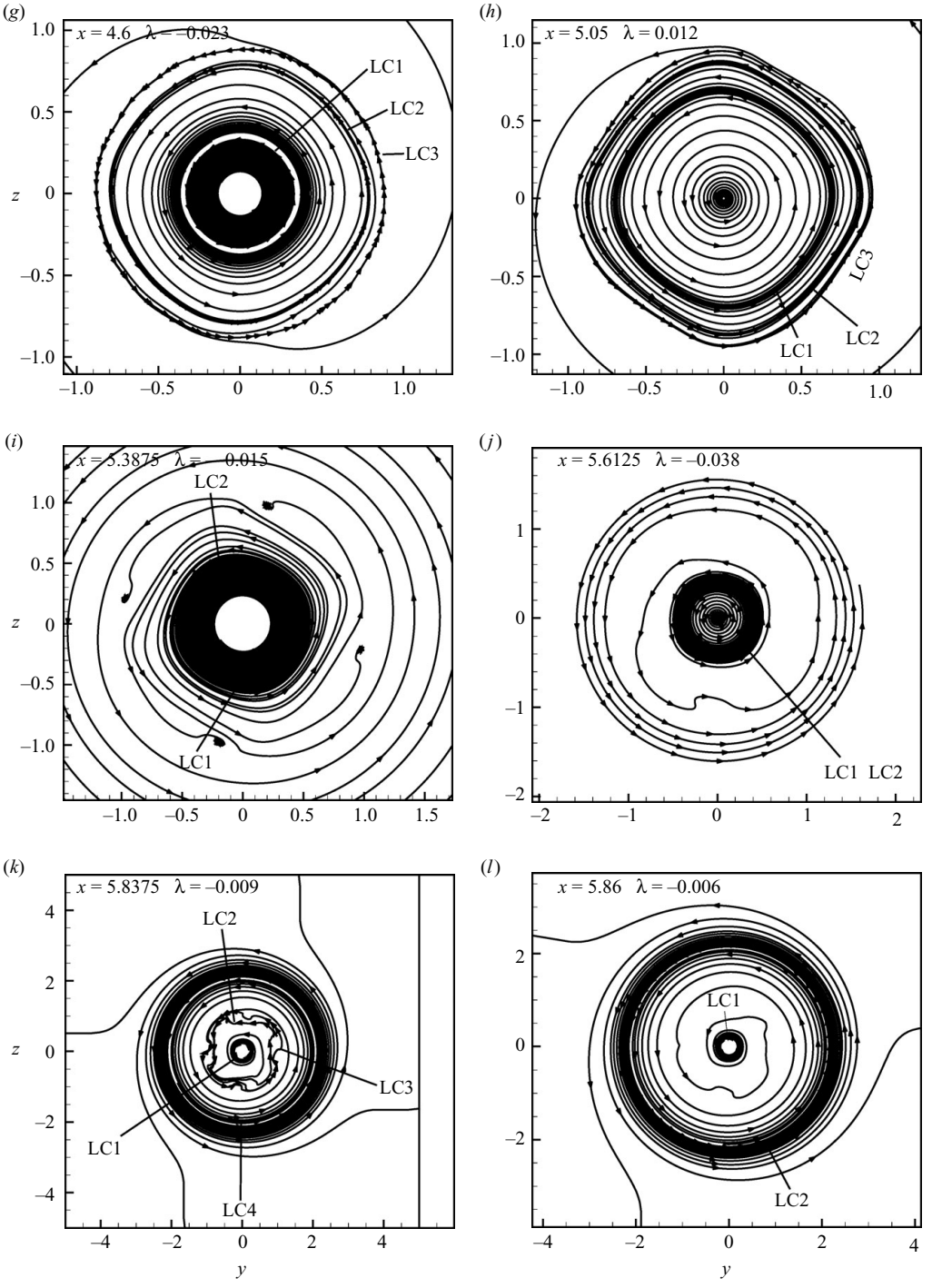

FIGURE 10. For caption see page 17

3.2.1. *The topological structure in the meridional plane*

Figure 12 contains the evolution of the shock structure in the meridional plane. At the beginning of the interaction, the initial shock is deformed to a bow shape. At the intersection point between the bow shock and the vortex axis, the shock

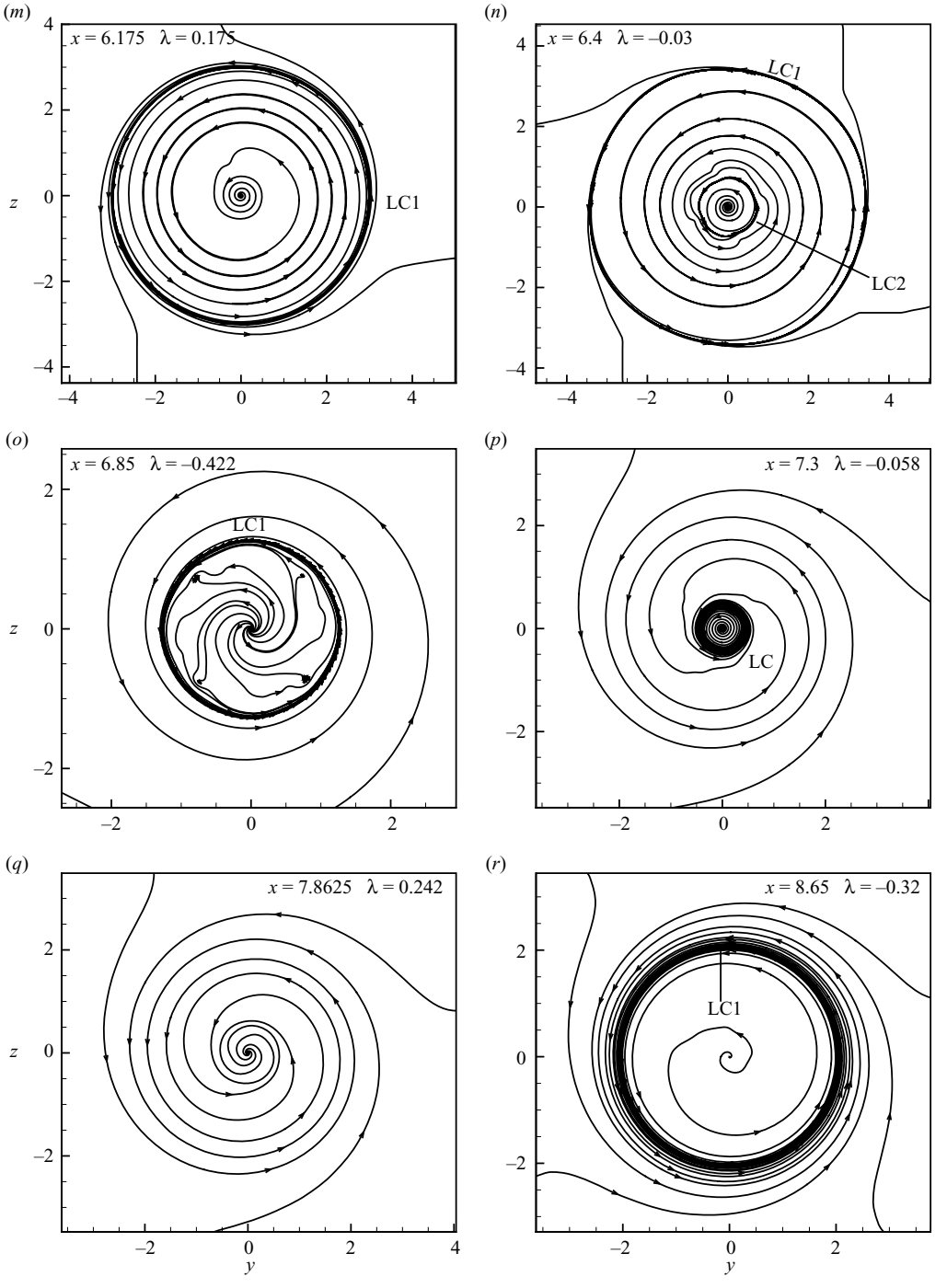

FIGURE 10. The sectional streamline pattern in the cross-section perpendicular to the vortex axis $t = 25$ of case I.

keeps perpendicular to the vortex axis. As time increases, the intersection point moves upwards continuously and there appears a triple point on the initial shock wave which moves upwards continuously. Another shock appears at approximately $x = 0$. At $t = 11$, the interaction results in a complex shock structure, which includes three

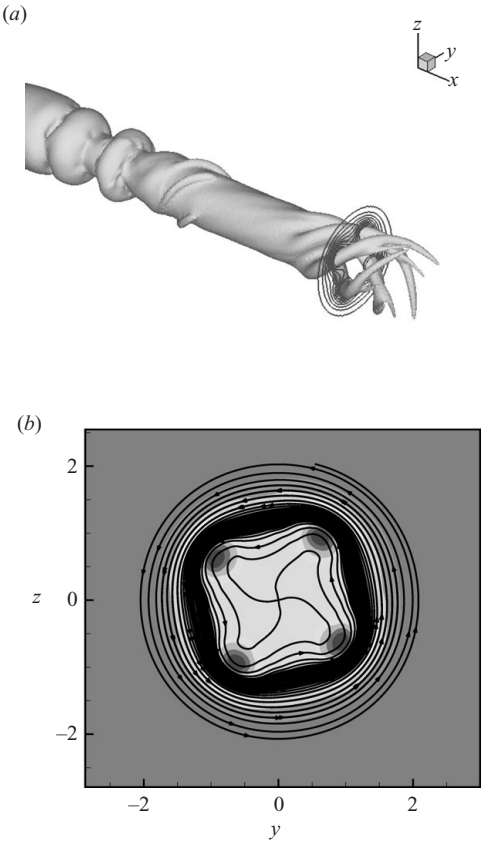

FIGURE 11. The iso-surface (a) of density $\rho = 1.2$ and the density contour and sectional streamlines on the cross-section of $x = 19.9$ (b) for Case I at $t = 25$.

oblique shock waves A, B and C and a normal shock wave D. H, E_1 and E_2 are shear layers. The positions of the shock waves are the same as those obtained by Erlebacher *et al.* (1997) from the axisymmetrical Euler equations.

Figure 13 contains the sectional streamlines in the meridional plane at typical times, which represent the onset and time evolution of the shock induced vortex breakdown. It can be seen from figure 13(a) that the vortex breakdown begins at a combination of a saddle and a node on the vortex axis, which is the same with the topological analysis shown in figure 4. After that, a reversal flow bubble appears just after the deformed shock. As time increases, the bubble becomes larger. At the tail of the breakdown region, there are a series of small vortices similar to the structure of a shear layer.

Figure 14 contains the three-dimensional streamlines (figure 14a) and iso-vorticity surface (figure 14b). From the figure of the three-dimensional streamlines, we can observe a vortex ring near $x = 0$. Similar to Case I described in the previous subsection, we observe again a quadru-helix structure in the tail of the vortex breakdown. In figure 15 we plot the iso-surface of vorticity as well as the density contour on a cross-section in the tail of the vortex breakdown. We observe that the quadru-helix structure can match with the density contours. In figure 16, we plot the iso-surface of density $\rho = 1.75$ and the three-dimensional streamlines starting from the tails of the

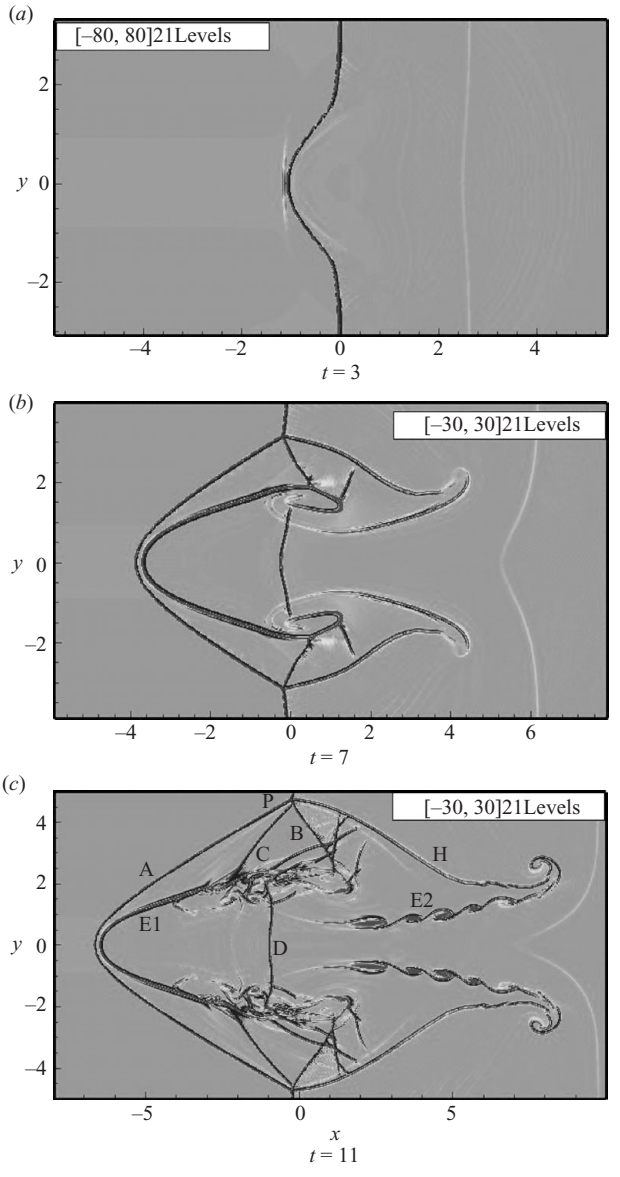

FIGURE 12. The time evolution of flow structure in the meridional plane for $M_1 = 2$ and $\epsilon = 7$: numerical shadowgraph obtained from $\nabla^2\rho = \partial^2\rho/\partial x^2 + \partial^2\rho/\partial y^2$.

quadru-helix. We can observe that each leg of the quadru-helix structure corresponds exactly to a small vortex tube. Comparing the iso-density surface and the iso-vorticity surface, we can observe similar flow structures represented, however the iso-vorticity surface seems much clearer to show small scale vortices than the iso-density surface. Due to the limitation on the speed and memory of our visualization software, all three-dimensional figures are plotted from the simulation data by skipping some grid points. A detailed comparison of the two visualizing techniques is left for future study.

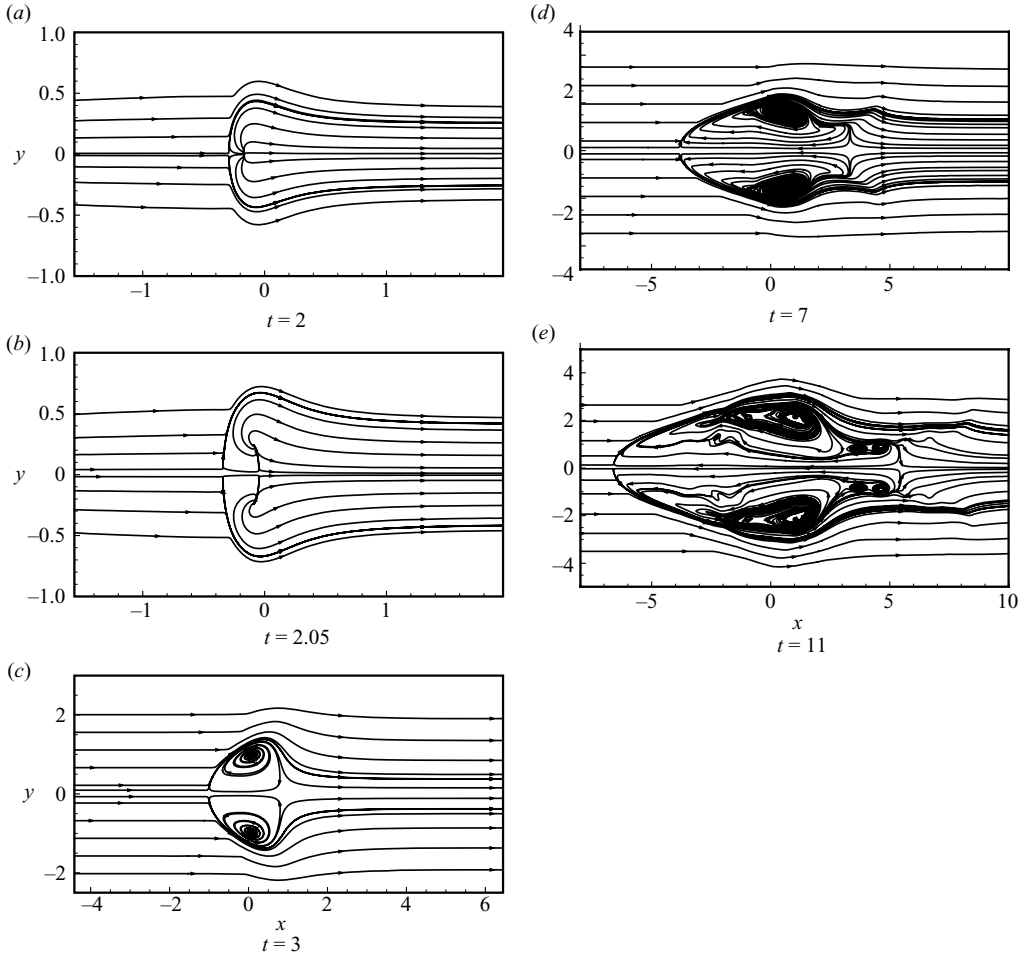

FIGURE 13. The sectional streamline pattern and its time evolution in the meridional plane for $M_1 = 2$ and $\epsilon = 7$.

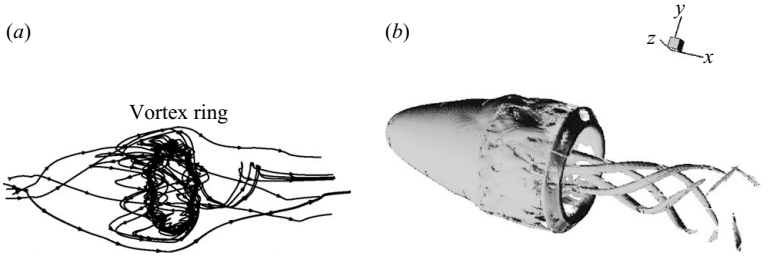

FIGURE 14. Three dimensional streamlines (a) and iso-vorticity surface $|\omega| = 9$ (b) at $t = 11$ for Case II.

3.2.2. *The sectional streamline pattern in the cross-section perpendicular to the vortex axis*

Figure 17 is the distribution of $\lambda(x, t)$ along the vortex axis at $t = 11$. In this case, there are three positive λ regions p_1, p_2 and p_3 and three negative λ regions n_1, n_2

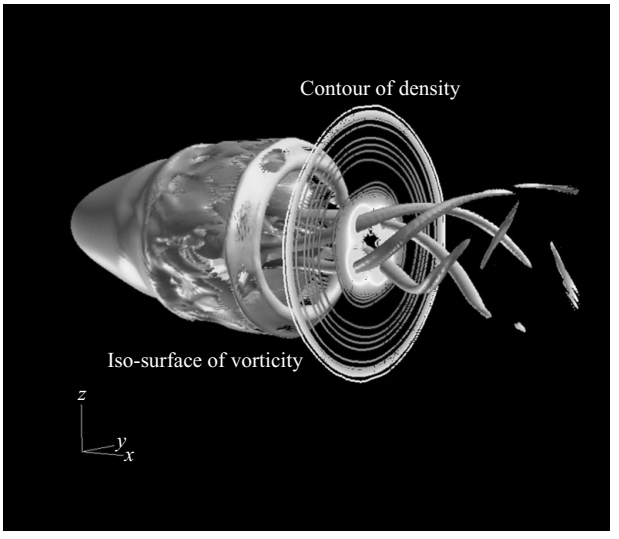

FIGURE 15. The iso-surface of vorticity $|\omega| = 9$ and the contour of density on the cross-section $x = 3.52653$ for Case II.

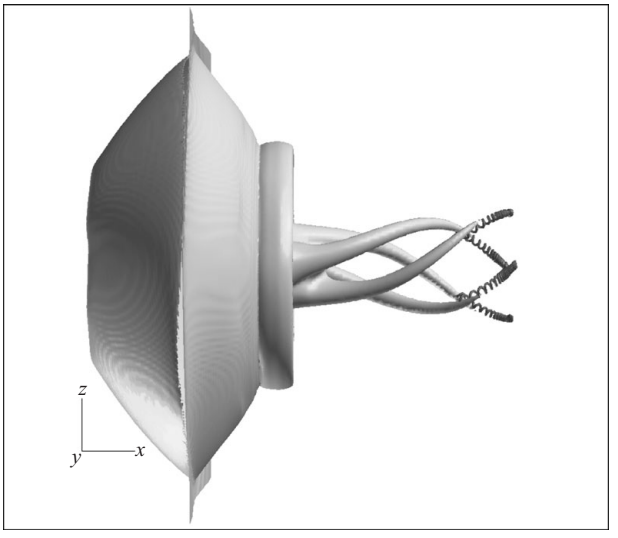

FIGURE 16. The iso-surface of density $\rho = 1.75$ and three-dimensional streamlines (in red) at $t = 11$ for Case II.

and n_3. Figure 18 contains the sectional streamlines in the cross-section perpendicular to the vortex axis.

From figure 18, we obtain the same conclusion as in Case I: (i) In the region of $\lambda > 0$, the sectional streamline in the vicinity of the vortex core spirals inwards; (ii) in the region of $\lambda < 0$, the sectional streamline in the vicinity of the vortex core spirals outwards; (iii) one or more limit cycles appear when λ changes its sign. Similar to Case I, we find four small vortices in the circumferential direction at $x = -2.6$ which might be the origin of the quadru-helix structure. At the cross-section of $x = -2.52125$, there are a series of critical points on the third limit cycle (see figures 18*g* and 18*h*). The pattern of the critical points consists of saddles or nodes. The saddles

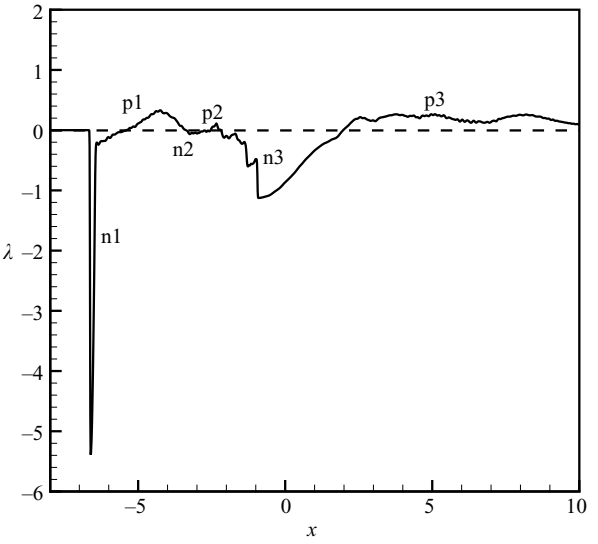

FIGURE 17. The distribution of λ on the vortex axis at $t = 11$ of Case II.

and nodes are distributed alternately. Figure 19 shows the density contours in this section. We can observe that there are a lot of small structures around the third limit cycle, which is a turbulence-like shear layer. Along this turbulence-like shear layer, the sectional streamlines in figures 18(g), 18(h) and 18(i) are very complicated. Even though there are a lot of small scale structures that we cannot fully resolve, the larger scale structures are approximately grid independent. Figure 20 contains the circumferential distribution of density at $r = 1.382$ and $r = 1.848$ on the cross-section of $x = -2.6$. Figure 21 contains the radial distribution of density along the positive y-axis. From these two figures, we can observe a significant difference between the results obtained by the finest and the coarsest grids. However, the results obtained by the finest grid (Grid1) and the medium grid (Grid2) agree reasonably well. The key difference is in the smallest scale structures. This means that our numerical results are approximately grid-independent for large-scale structures.

3.3. *Double Hopf bifurcation of swirling flow and multi-helix structure of vortex breakdown*

Through the numerical simulation for the interaction of a normal shock and a longitudinal vortex, we found that there is a quadru-helix structure in the tail of the vortex breakdown. In fact, this phenomenon has close relationship with the instability of the rotating waves.

Through a linear stability analysis, Sanchez *et al.* (2002) and Marques *et al.* (2003) studied the stability of azimuthal waves for a swirling flow. They found that the most unstable modes are $m = 4$ and 8, which result in the tangent Hopf bifurcation of the axisymmetric basic state.

In the interaction between a normal shock and an axisymmetric vortex, the Reynolds number is very large. It is also the azimuthal instability that results in the difference between the result obtained from a full three-dimensional Navier–Stokes simulation and a simulation based on the axisymmetric equations.

Figure 22 contains the circumferential distribution around a circle and their Fourier transformation. The density is obtained at the cross-section of $x = 5.8375$

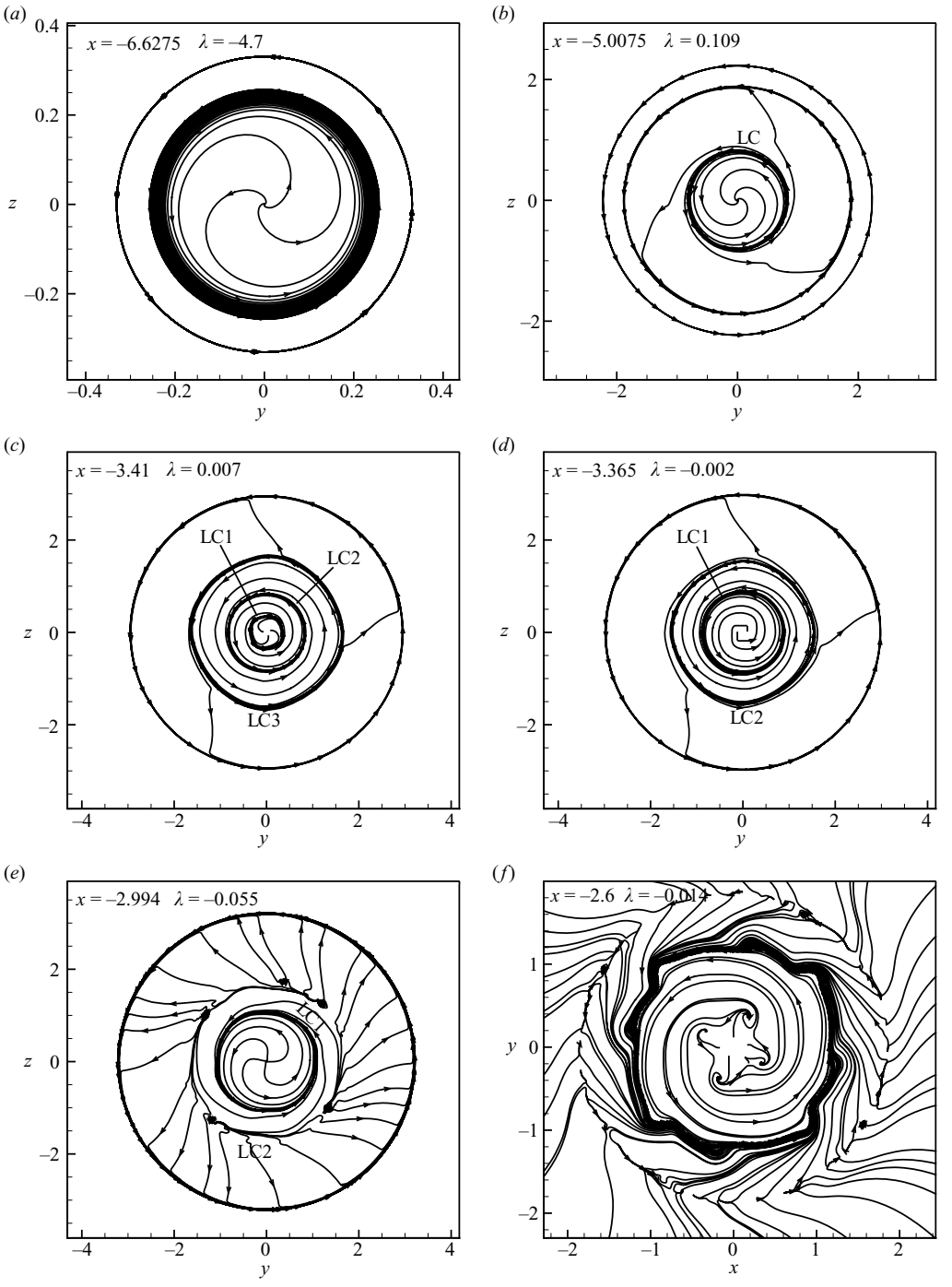

FIGURE 18. For caption see next page.

and $r = 1.0143$ for Case I and of $x = 4.6$ and $r = 0.83246$ for Case II. In both cases, we found that $m = 4$ and 8 are the two most unstable azimuthal wave modes. In the cross-section of Case II, we can observe the $m = 4$ mode at the cross-section of $x = -3.41$ (see figure 18*c*), which develops into four small vortices (see figure 18*f*). The

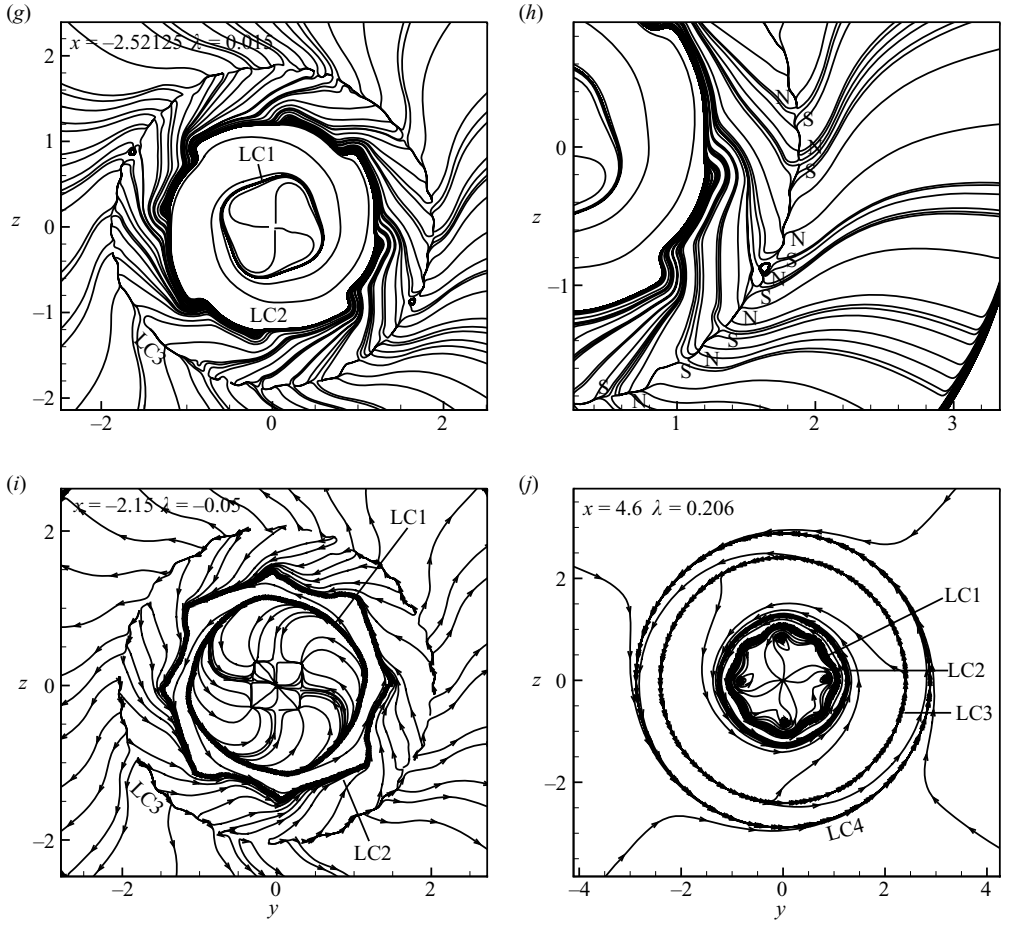

FIGURE 18. The sectional streamline pattern in the cross-section perpendicular to the vortex axis $t = 11$ of Case II.

mode of $m = 8$ can be observed at the cross-section of $x = -2.6$ shown in figure 18(f). If the four small vortices represent the four vortex tubes in the tail of the vortex breakdown in figure 14, we can predict that there are also eight helix in the tail of the vortex breakdown, which is not visualized due to the limitation of the numerical visualization. Hence, the vortex breakdown has a multi-helix structure.

3.4. *Discussion on flow visualization*

In this section we give a brief discussion on flow visualization and a justification of using sectional streamlines to reveal flow structures.

Plotting density contours on cross-sections is a common method to view the structure of a three-dimensional flow, which is similar to the Mach contours on a cross-section (Kandil *et al.* 1992). Figure 23 is a three-dimensional iso-surface of density and the density contours on a cross-section for Case II discussed in § 3.2. We can observe that the density contour on the cross-section can match the three-dimensional structure of density iso-surface.

In our simulating cases, the sectional streamlines can match the contours of the density. In figure 24, we plot the contours of density and the sectional streamlines on two typical cross-sections of $x = -2.6$ and $x = 4.6$ for Case II discussed in § 3.2.

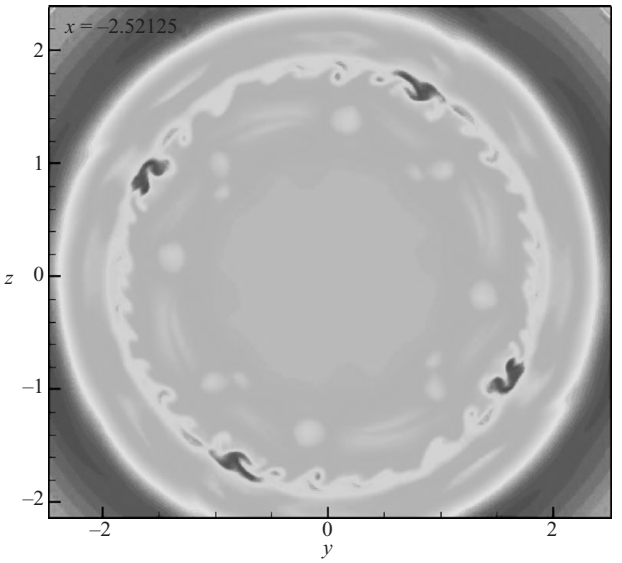

FIGURE 19. The contours of density in the cross-section perpendicular to the vortex axis at $x = -2.5125$ of Case II.

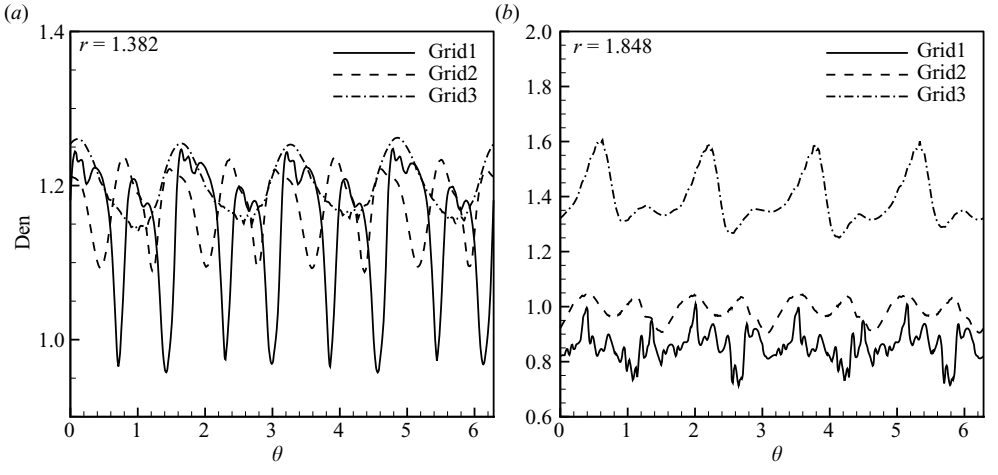

FIGURE 20. The circumferential density distribution and a comparison among different grids at the cross-section of $x = -2.6$ of Case II. (*a*) $r = 1.382$; (*b*) $r = 1.848$.

We can observe that the sectional streamlines and density contours describe the same flow structure, while the former can better reveal vortex structures including swirling direction.

The flow of a normal shock and a longitudinal vortex interaction is asymmetric. However, they are developed from an axisymmetric flow and certain symmetry are still maintained in the three-dimensional simulation. We plot the density contours in the x–y plane and the x–z plane and find that they are identical (not shown here to save space). This justifies our specific choice of sectional streamlines to visualize. Figure 25 contains the sectional streamlines on the meridional plane (x–z plane) and density contours. They reveal the same flow structure, while again the former can better reveal vortex structures including swirling direction.

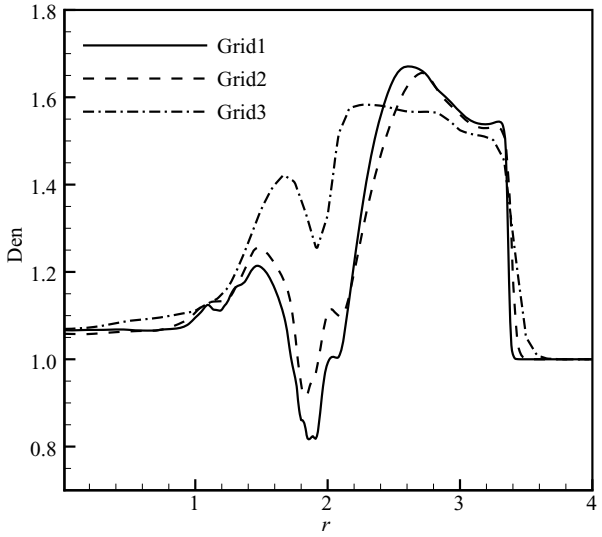

FIGURE 21. The radial density distribution and a comparison among different grids at the cross-section of $x = -2.6$ of Case II.

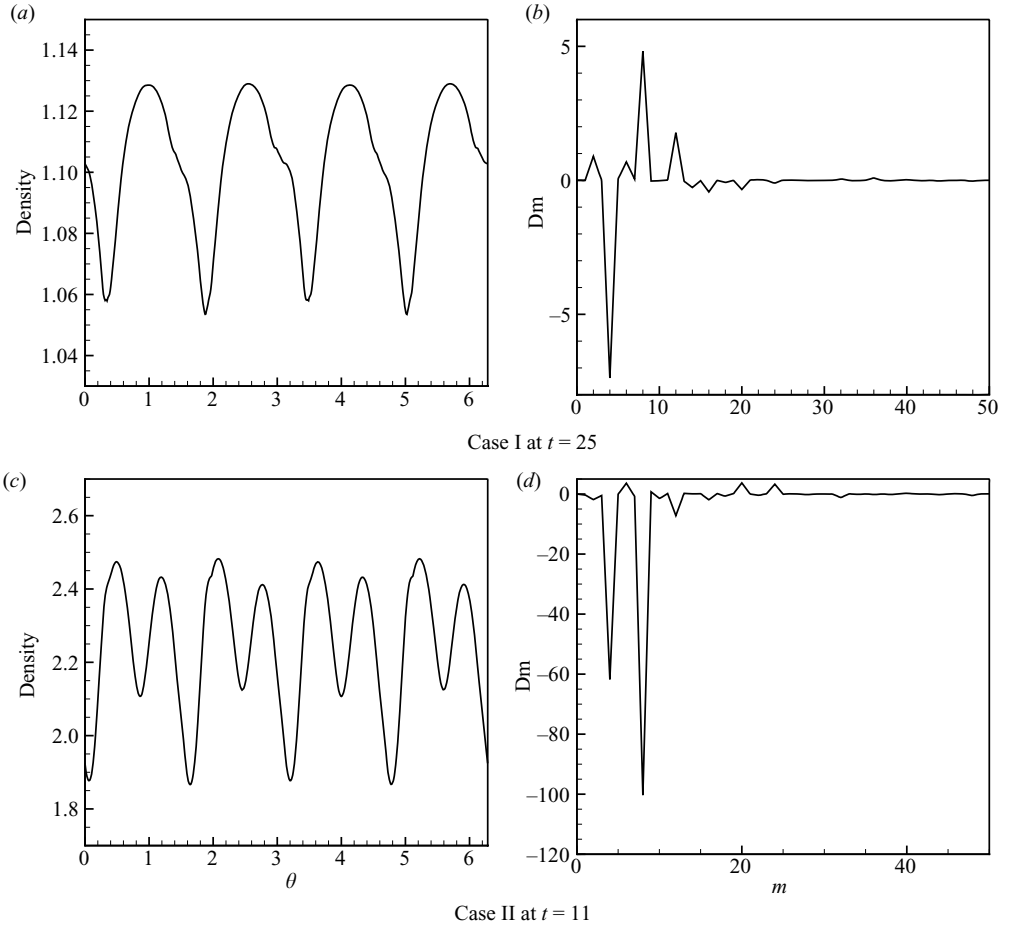

FIGURE 22. The circumferential density distribution (a, c) and its Fourier transformation (b, d).

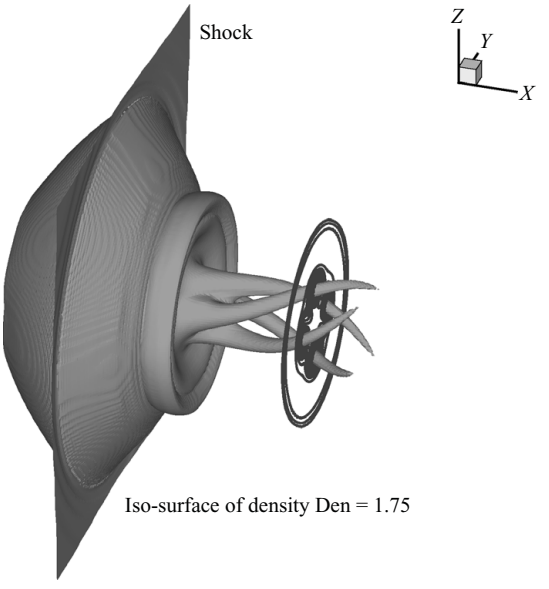

FIGURE 23. The iso-surface of density $\rho = 1.75$ and the contour of density on a cross-section for Case II.

4. Concluding remarks

Based on the critical point theory of ordinary differential equations, we have studied the topological structure of a swirling flow. The topological structure contains the sectional streamline pattern in the symmetric plane and in the cross-section perpendicular to the vortex axis. In the cross-section perpendicular to the vortex axis, the sectional streamline pattern in the vicinity of the vortex core can be of two types, spiral inwards and spiral outwards, depending on a function $\lambda(x,t) = 1/\rho(\partial\rho/\partial t + \partial\rho u/\partial x)$. If $\lambda > 0$, the sectional streamline spirals inwards. If $\lambda < 0$, the sectional streamline spirals outwards. If λ changes its sign along the vortex axis and the sectional streamlines far away from the vortex core do not change their spiral direction, one or more limit cycles appear in the sectional streamline in the cross-section perpendicular to the vortex axis.

For a steady flow, there is an essential difference between a supersonic and a subsonic vortex. For a supersonic vortex, sectional streamlines in the vicinity of the vortex core spiral outwards in the locally favourable pressure region. They spiral inwards in the locally adverse pressure region. For a subsonic vortex, sectional streamlines in the vicinity of the vortex core spiral inwards in the locally favourable pressure region and spiral outwards in the locally adverse pressure region.

Unlike the steady case, there are two types of critical points on the vortex axis for an unsteady flow. They are saddles and nodes.

Two typical interactions of a normal shock wave and a longitudinal vortex are simulated by solving the three-dimensional unsteady Navier–Stokes equations. The shock induced vortex breakdown is obtained. Numerical results agree with the topological analysis. In the region of $\lambda > 0$, sectional streamlines in the vicinity of the vortex core spiral inwards. In the region of $\lambda < 0$, sectional streamlines in the vicinity of the vortex core spiral outwards. More limit cycles are found in the sectional streamline pattern of the cross-section perpendicular to the vortex core when λ changes its sign along the vortex axis.

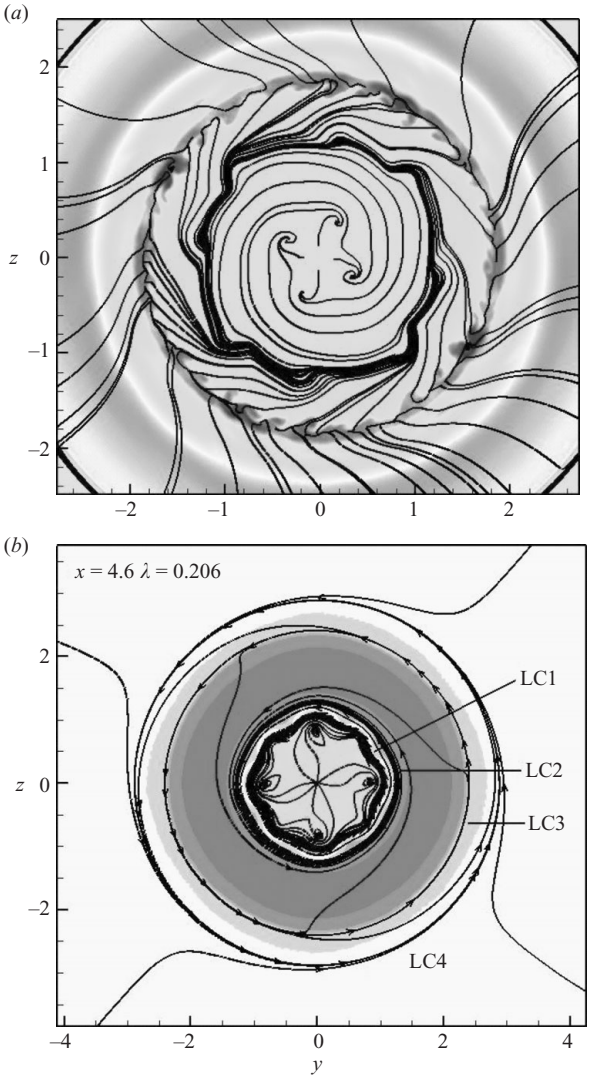

FIGURE 24. The contour of density and sectional streamlines on the cross-sections of $x = -2.6$ (a) and $x = 4.6$ (b) for Case II at $t = 11$.

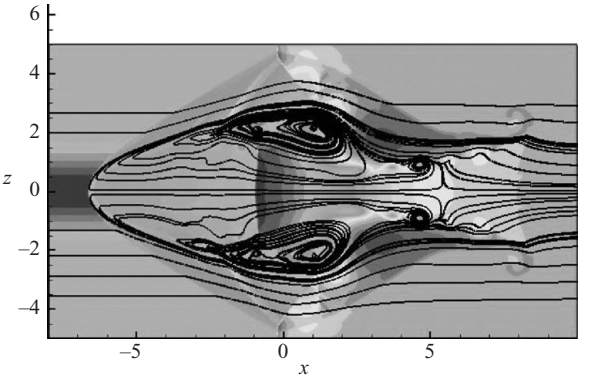

FIGURE 25. The density contour and sectional streamlines on the x–z plane for Case II at $t = 11$.

A quadru-helix structure is found in the tail of the vortex breakdown, which results from the instability of the azimuthal wave with $m = 4$. Using Fourier analysis, we found that there are more unstable waves. Hence, we predict that the vortex breakdown has a multi-helix structure.

REFERENCES

Benjamin, T. B. 1962 Theory of the vortex breakdown phenomenon. *J. Fluid Mech.* **14**, 593–629.

Bisset, D., Antonia, R. & Browne, L. 1990 Spatial organization of large structures in the turbulent far wake of a cylinder. *J. Fluid Mech.* **218**, 439–461.

Blackmore, D. 1994 Simple dynamical models for vortex breakdown of B-type. *Acta Mech.* **102**, 91–101.

Blackmore, D., Brøns, M. & Goullet, A. 2008 A coaxial vortex ring model for vortex breakdown. *Physica* D. **237**, 2817–2844.

Bossel, H. H. 1969 Vortex breakdown flow field. *Phys. Fluids* **12**, 498–508.

Brøns, M., Shen, W. Z., Sørensen, J. N. & Zhu, W. J. 2007 The influence of imperfections on the flow structure of steady vortex breakdown bubbles. *J. Fluid Mech.* **578**, 453–466.

Brøns, M., Voigt, L. K. & Sørensen, J. N. 1999 Streamline topology of steady axisymmetric vortex breakdown in a cylinder with co- and counter-rotating end-covers. *J. Fluid Mech.* **401**, 275–292.

Brücker, C. & Althaus, W. 1995 Study of vortex breakdown by particle tracking velocimetry (PTV). Part 3. Time-dependent structure and development of breakdown-modes. *Exp. Fluids* **18**, 174–186.

Chong, M. S., Perry, A. E. & Cantwell, B. J. 1990 A general classification of three-dimensional flow field. *Phys. Fluids* A **2**, 765.

Crank, J., Martin, H. G. & Melluish, D. M. 1977 *Nonlinear Ordinary Differential Equations.* Oxford University Press.

Delery, J. M. 1994 Aspects of vortex breakdown. *Prog. Aerosp. Sci.* **30**, 1–59.

Erlebacher, G., Hussaini, M. Y. & Shu, C.-W. 1997 Interaction of a shock with a longitudinal vortex. *J. Fluid Mech.* **337**, 129–153.

Escudier, M. P. 1984 Observations of the flow produced in a cylindrical container by a rotating endwall. *Exp. Fluids* **2**, 189–196.

Faler, J. H. & Leibovich, S. 1977 Disrupted states of vortex flow and vortex breakdown. *Phys. Fluids* **20**, 1385–1400.

Hall, M. G. 1961 A theory for the core of a leading-edge vortex. *J. Fluid Mech.* **11**, 209–228.

Hall, M. G. 1967 A new approach to vortex breakdown. *Proceedings of the 1967 heat transfer and fluid mechanics institute,* University of California, San Diego, La Jolla.

Haller, G. 2004 Exact theory of unsteady separation for two-dimensional flows. *J. Fluid Mech.* **512**, 257–311.

Howard, L. N. & Gupta, A. S. 1962 On the hydrodynamic and hydromagnetic stability of swirling flows. *J. Fluid Mech.* **14**, 463–476.

Hunt, J. C. R., Abell, C. J., Peterka, J. A. & Woo, H. 1978 Kinematical studies of the flow around free or surface-mounted obstacles; applying topology to flow visualization. *J. Fluid Mech.* **86**, 179–200.

Hussain, A. & Hayakawa, M. 1987 Education of large-scale organized structures in a turbulent plane wake. *J. Fluid Mech.* **180**, 193–229.

Jeong, J. & Hussain, F. 1995 On the identification of a vortex. *J. Fluid Mech.* **285**, 69–94.

Jiang, G.-S. & Shu, C.-W. 1996 Efficient implementation of weighted ENO schemes. *J. Comput. Phys.* **126**, 202–228.

Kalkhoran, I. & Smart, M. 2000 Aspects of shock wave-induced vortex breakdown. *Prog. Aerosp. Sci.* **36**, 63–95.

Kandil, O., Kandil, H. & Liu, C. H. 1992 Shock/vortex interaction and vortex-breakdown modes. In *IUTAM Symposium of Fluid Dynamics of High Angle of Attack* (ed. R. Kawamura & Y. Aihara), pp. 192–212. Springer.

Klass, M., Schröder, W. & Thomer, O. 2005 Experimental investigation and numerical simulation of oblique shock/vortex interaction. In *Vortex Dominated Flows: A Volume Celebrating Lu Ting's 80th Birthday* (ed. D. Blackmore, E. Krause & C. Tung), pp. 119–134. World Scientific.

Krause, E., Thomer, O. & Schröder, W. 2003 Strong shock-vortex interaction – a numerical study. *Comput. Fluid Dyn.* **12**, 266–278.

Kurosaka, M., Cain, C. B., Srigrarom, S., Wimer, J. D., Dabiri, D., Johnson III, W. F., Hatcher, J. C., Thompson, B. R., Kikuchi, M., Hirano, K., Yuge, T. & Honda, T. 2006 Azimuthal vorticity gradient in the formative stages of vortex breakdown. *J. Fluid Mech.* **10**, 221–246.

Leibovich, S. 1978 The structure of vortex breakdown. *Annu. Rev. Fluid Mech.* **10**, 221–246.

Lessen, M., Singh, P. J. & Paillet, F. 1974 The stability of a trailing line vortex. Part 1. Inviscid theory. *J. Fluid Mech.* **65**, 753–763.

Marques, F., Gelfgat, A. Y. & Lopez, J. M. 2003 Tangent double Hopf bifurcation in a differentially rotating cylinder flow. *Phys. Rev.* E **68**, 016310.

Perry, A. E. & Chong, M. S. 1986 A series-expansion study of the Navier–Stokes equation with applications to three-dimensional separation patterns. *J. Fluid Mech.* **173**, 207–223.

Ruith, M. R., Chen, P., Meiburg, E. & Maxworth, T. 2003 Three-dimensional vortex breakdown in swirling jets and wakes: direct numerical simulation. *J. Fluid Mech.* **486**, 331–378.

Sanchez, J., Marques, F. & Lopez, J. M. 2002 A continuation and bifurcation technique for Navier–Stokes flows. *J. Comput. Phys.* **180**, 78–98.

Sarpkaya, T. 1971 On stationary and travelling vortex breakdown. *J. Fluid Mech.* **45**, 545–559.

Spall, R. E. 1996 Transition from spiral- to bubble-type vortex breakdown. *Phys. Fluids* **8**, 1330–1332.

Surana, A., Grunberg, O. & Haller, G. 2006 Exact theory of three-dimensional flow separation. Part 1. Steady separation. *J. Fluid Mech.* **564**, 57–103.

Tobak, M. & Peake, D. J. 1982 Topology of three-dimensional separated flows. *Annu. Rev. Fluid Mech.* **14**, 61–85.

Werle, H. 1954 Quelques Résultats expérimentaux sur les ailes en Fleches, aux faibles vitesses. Obtenus en tunnel hydrodynamique. *La Recherche Aéronautiale.* **41**, 15–21.

Zhang, H. 1995 Characteristic analysis of subsonic and supersonic vortical flow. *ACTA Aerodyn. Sin.* **13**, 259–264 (in Chinese).

Zhang, S. & Shu, C.-W. 2007 A new smooth indicator for the WENO schemes and its effect on the convergence to steady state solutions. *J. Sci. Comput.* **31**, 273–305.

Zhang, S., Zhang, Y.-T. & Shu, C.-W. 2005 Multistage interaction of a shock wave and a strong vortex. *Phys. Fluids* **17**, 116101.

Zhang, S., Zhang, Y.-T. & Shu, C.-W. 2006 Interaction of an oblique shock wave with a pair of parallel vortices: shock dynamics and mechanism of sound generation. *Phys. Fluids* **18**, 126101.

Zhang, S., Zhang, H. & Zhu, G. 1996 Numerical simulation of vortex structure in the leeside of supersonic delta wing. *ACTA Aerodyn. Sin.* **14**, 430–435 (in Chinese).

Zhang, S., Zhang, H. & Zhu, G. 1997 Numerical simulation of vortical flows over delta wings and analysis of vortex motion. *ACTA Aerodyn. Sin.* **15**, 121–129 (in Chinese).

Zhang, S. & Zhu, G. 1997 Numerical visualization for three-dimensional vortex. In *Fifth triennial international symposium on fluid control, measurement and visualization*, Hayama, Japan.